INTERCOMPARISON OF METHODS TO APPLY SATELLITE OBSERVATIONS FOR INVERSE MODELLING OF NO_x SURFACE EMISSIONS

by

Akhila L. Padmanabhan

Submitted in partial fulfilment of the requirements
for the degree of Master of Science

at

DalhousieUniversity
Halifax, Nova Scotia
September 2013

Table of Contents

List of Figures

Abstract

Knowledge of NO_x (NO_2 + NO) emissions is useful to understand processes affecting air quality and climate change. Emission inventories of surface NO_x have high uncertainties. Satellite remote sensing has enabled measurements of trace gases in the atmosphere over a large regional and temporal scale. Inverse modeling of NO_2 observations from satellites can be used to improve existing emissions inventories. This study seeks to understand the difference in two methods of inverse modeling: the mass balance approach and the adjoint approach using the GEOS-Chem chemical transport model and its adjoint. Using both synthetic satellite observations and those derived from the SCIAMACHY satellite instrument, this paper found that the performance of these two inversions was affected by pixel smearing and observational error. Smearing reduced the accuracy of the mass balance approach, while high observational error reduced the accuracy of the adjoint approach. However, both approaches improved the *a priori* emissions estimate.

List of Abbreviations Used

4DVAR	Four- Dimensional Variational Calculus
AMF	Air Mass Factor
BRAVO	Big Bend Regional Aerosol and Visibility Observational Study
CAC	Criteria Air Contaminants
CH_3O_2	Methylperoxyradical
CH_3O	Methoxy Radical
CTM	Chemical Transport Model
EDGAR	Emissions Database for Global Atmospheric Research
EMEP	European Monitoring and Evaluation Programme
EPA/NEI99	Environmental Protection Agency/ National Emissions Inventory 99
FRESCO	Fast Retrieval Scheme for Cloud Observations
GEOS-Chem	Goddard Earth Observing System Chemical Transport Model
GFED	Global Fire Emissions Database
GOME2	Global Ozone Monitoring Experiment
HNO_3	Nitric Acid
HO_2	Hydroperoxy Radical
KPP	Kinetic Pre-Processor
L-BFGS	Limited Memory Broyden-Fletcher-Goldfarb-Shanno method
LIDORT	Linearized Discrete Ordinate Radiative Transfer model
M	A third body that stabilizes the reaction by collision
NME	Normalized Mean Error
NO	Nitrogen Oxide Radical
NO_2	Nitrogen Dioxide Radical
NO_3	Nitrogen Trioxide Radical
NO_x	Nitrogen Oxide+ Nitrogen Dioxide Radical
N_2O_5	DinitrogenPentoxide
O^1D	Excited state of the oxygen radical
O_2	Oxygen
O_3	Ozone
OH	Hydroxyl Radical
PAN	peroxyacetylnitrate $CH_3COOONO_2$
R	a hydrocarbon
RH	a hydrocarbon
R'	an organic chain with one less carbon than R
SCIAMACHY	SCanning Imaging Absorption SpectroMeter for Atmospheric CHartographY
TAMC	Tangent and Adjoint Model Compiler
VCD	Vertical Column Density

Acknowledgements

I would like to thank my supervisory committee, Dr. Peter Wentzell, Dr. Jeffrey Pierce, and Dr. Randall Martin for their guidance. I would especially like to thank my supervisor, Dr. Randall Martin, for his unfaltering support, endless patience, and ongoing encouragement. I would also like to thank my colleagues in Dr. Martin's group for all of their insight and help. I would especially like to acknowledge Colin Lee and Dr. Aaron Van Donkelaar for all the "tutorials" they gave me. Thank you to Daven Henze and Dr. Nicolas Bousserez from the University of Colorado. I am grateful to NSERC and Dalhousie University for funding this research. Finally I would like to send out a very special thank you to Jeremy, Maya, and Laila for being my inspiration

Chapter 1 Introduction

1.1 Motivation

Emissions of nitrogen oxides, (NO_x =NO and NO_2), play a major role in air quality and climate change. NO_x serves as a catalyst for the production of tropospheric ozone, a greenhouse gas that directly affects the Earth's radiation budget [*Forster et al.,* 1997]. Nitrogen dioxide affects human health and mortality [*Burnett et al.*, 2004]. Sources of NO_x emission into the troposphere include fossil fuel combustion, soil, biomass burning, and lightning. Direct inference of emissions is impeded by sparse *in situ* measurements. However, satellites are able to provide broad spatial and temporal perspectives that should improve our understanding of emissions.

Researchers aggregate information about NO_x emissions, such as fuel and land use statistics, emissions records, and direct measurements, to create "bottom-up" emissions inventories. Climate models, which are used in various applications, rely on these emissions inventories as inputs. But these inventories have a great deal of uncertainty associated with them. And although there are also uncertainties in other model parameters, such as chemistry and deposition, emissions uncertainties can drive the errors in the model. Furthermore, the emissions inventories are often for previous years and must be scaled in order to reflect current time periods.

NO_x is emitted into the troposphere primarily as nitric oxide (NO). It then reacts with tropospheric ozone to produce nitrogen dioxide (NO_2), which is subsequently photolysed back to NO. This rapid cycling between the two species reaches steady- state within minutes. The major sink for NO_x in the troposphere is through oxidation. During the day, the hydroxyl radical is formed through photolysis and oxidizes NO_2 to HNO_3 which is subsequently removed through wet deposition.

Satellites are able to measure tropospheric NO_2 concentrations over large spatial and temporal scales. These measurements can provide a "top-down" constraint for emissions inventories. Using these satellite measurements of NO_2 in combination with knowledge of emissions sources and vertical distribution of NO_x allows for inferences to be made about NO_x emissions through inverse modeling.

There have been various methods of inverting NO_2 satellite measurements used to improve NO_x emissions inventories. Techniques such as a mass balance approach (e.g. *Martin et al.*, 2003, 2006, *Jaegle et al.*, 2005, *Wang et al.*, 2007) and multivariate linear regression (e.g. *Lin* ,2012) have been used to invert NO_2 vertical column densities (VCD), creating a "top-down" estimate of NO_x emissions that can be combined with the "bottom-up" or *a priori* estimate. Both of these techniques assume that the transport of NO_x across spatial grid boxes could be neglected due to the short life-time of NO_x. However sensitivity studies show that non-local sources contribute to the tropospheric NO_2 columns, even those averaged over larger spatial regions (*Turner et al.*, 2012). Four- dimensional variational (4DVAR) data assimilation and Kalman filters, which take into account feedbacks from non-local sources of NO_2 have also been used in inversions (*Napelenok et al.*, 2008, *Mijling et al.*, 2012, *Kurokawa et al.*, 2009). These data assimilation techniques are computationally expensive and can take days or even weeks, to solve inversion problems. The present study seeks to further understand the differences between the mass balance and 4DVAR methods of NO_2 inverse modeling and each techniques advantages and disadvantages.

1.2 Background Information

The following section discusses some background information related to NO_x chemistry, chemical transport models, inverse modeling and the mass balance and 4DVAR techniques.

1.2.1 NO_x Chemistry

The primary anthropogenic sources of NO_x include combustion of fossil fuels from power generation, automobiles, and biomass burning. Natural sources include lightning, forest fires, and soil emissions. NO_x is emitted primarily as NO and is quickly converted into NO_2 in the following cycle:

$$NO + O_3 \rightarrow NO_2 + O_2 \qquad \text{(R1)}$$

$$NO_2 + h\nu \xrightarrow{O_2} NO + O_3 \qquad \text{(R2)}$$

The inter-conversion between NO and NO_2 reaches steady state within minutes. Reaction R1 has a temperature dependence which results in NO_2 as the dominant species in the lower troposphere, from the surface to the boundary layer and NO in the upper troposphere, from the boundary layer to the tropopause.

During the day the primary sink for tropospheric NO_x is through oxidation into nitric acid followed by wet deposition.

$$NO_2 + OH + M \rightarrow HNO_3 + M \qquad \text{(R3)}$$

The hydroxyl radical, OH, is produced through photolysis of ozone. Therefore at night NO_x undergoes a different loss mechanism.

$$NO_2 + O_3 \rightarrow NO_3 + O_2 \qquad \text{(R4)}$$

$$NO_3 + NO_2 + M \rightarrow N_2O_5 + M \qquad \text{(R5)}$$

$$N_2O_5 + H_2O \xrightarrow{\text{aerosol}} 2HNO_3 \qquad \text{(R6)}$$

The lifetime of NO_x is approximately one day. Because of the short lifetime of NO_x, long range transport can only be achieved through the conversion into the species peroxyacetylnitrate, known as PAN, $CH_3COOONO_2$. When carbonyl compounds in the atmosphere undergo photochemical oxidation in the presence of NO_x, PAN is formed. This molecule has a lifetime of months at lower temperatures and is not highly soluble in water. Therefore, PAN can be transported over long distances in the upper troposphere. At warmer temperatures, PAN decomposes and NO_2 is released.

When there is a background of hydrocarbons in the troposphere, NO_x catalyses O_3 production. The HO_2 radical and the methylperoxy radical, CH_3O_2, are produced through the carbon monoxide and methane oxidation mechanisms. NO can react with these species, instead of O_3 in reaction R1, to form NO_2.

$$HO_2 + NO \rightarrow OH + NO_2 \qquad \text{(R7)}$$

$$CH_3O_2 + NO \rightarrow CH_3O + NO_2 \qquad \text{(R8)}$$

The cycle of reaction R1 andR2 is a null cycle for both NO_x and O_3, meaning neither species is produced or lost in the net reaction. However if reaction R7 or R8 were to occur instead of reaction R1, O_3 would be produced.

Although O_3 in the stratosphere is important for filtering UV radiation, at the earth's surface it is a pollutant. In highly populated areas where both NO_x and hydrocarbons are emitted, surface ozone pollution is a problem. The cycle for ozone production is initiated by the formation of the hydroxyl radical:

$$O_3 + h\nu \rightarrow O_2 + O(^1D) \quad \text{(R9)}$$

$$O(^1D) + H_2O \rightarrow 2OH \quad \text{(R10)}$$

Ozone is photolysed into an oxygen radical in an excited state (O^1D), which reacts with water in the atmosphere. The cycle is then propogated by the presence of NO_x and hydrocarbons (where *R* is an organic group in the hydrocarbon *R*H).

$$RH + OH + O_2 \rightarrow RO_2 + H_2O \quad \text{(R11)}$$

$$RO_2 + NO \rightarrow RO + NO_2 \quad \text{(R12)}$$

$$RO + O_2 \rightarrow R'CHO + HO_2 \quad \text{(R13)}$$

$$HO_2 + NO \rightarrow OH + NO_2 \quad \text{(R14)}$$

The NO_2 produced in reactions R12 and R14 subsequently photolyses as shown in reaction R2 to produce O_3. Therefore each repetition of this cycle produces 2 O_3 molecules. The cycle can be terminated after reactions R13 and R14 in the following ways:

$$HO_2 + HO_2 \rightarrow H_2O_2 + O_2 \quad \text{(R16)}$$

$$NO_2 + OH + M \rightarrow HNO_3 + M \quad \text{(R17)}$$

The more number of cycles that NO_x goes through before ultimately converting into HNO_3, the higher amount of ozone produced. From this perspective, NO_x can be seen as a driver for ground level ozone production. This makes understanding of NO_x emissions especially important to this problem.

Another issue that arises from NO_x emissions is aerosol formation. Nitric acid can condense in the atmosphere when combined with water and substances such as ammonia. Therefore, it is a precursor for aerosol particles. Aerosol particles affect the earth's radiation budget by scattering incoming solar light. They also provide nuclei for cloud condensation. The clouds that are formed in polluted areas have a larger albedo, which also decreases the incoming solar radiation. Aerosols also reduce visibility, creating a haze over the area covered.

1.2.2 Chemical Transport Models (CTMs)

The concentration of a chemical species in the atmosphere is governed by four processes: emissions, chemistry, transport, and deposition. A chemical transport model simulates these processes. Emissions are a source of a chemical species into an atmosphere and may be anthropogenic or biogenic. Chemistry involves the reactions that cause production or loss of a chemical species. An example of chemical loss is the oxidation of NO_2 by the hydroxyl radical to produce nitric acid. Transport is the flux of a chemical species due to wind. This can be caused by horizontal wind (advection) or vertical wind (turbulence). Chemical transport models assimilate meteorology input, which drives transport. Dry deposition is when the chemical species directly reacts and remains on the Earth's surface. Wet deposition involves scavenging by precipitation.

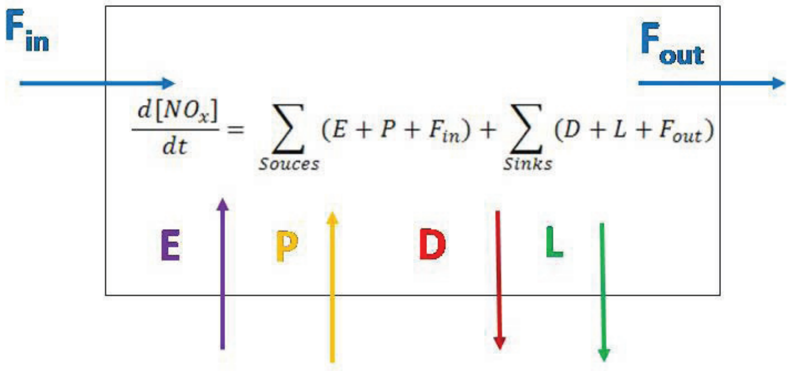

Figure 1.1: A one-box model showing the mass balance solution for the change in concentration of NO_x over time ($d[NO_x]/dt$) as the summation of sources minus the summation of sinks. F_{in} and F_{out} refer to the transport flux in and out of the box. P and L refer to the chemical production and loss. E refers to emissions and D refers to deposition.

Figure 1.1 shows a model that can be used to solve for a chemical species' concentration. The concentration of a species is the summation of the sources minus the summation of sinks. If all sources and sinks are known, the concentration can be solved for. In certain types of chemical transport models, the world is split into many three-dimensional boxes so a more sophisticated version of this mass-balance calculation is needed.

Chemical transport models (CTMs) solve for the concentration of a chemical species using the continuity equation. When the concentration is solved from a fixed frame of reference, the Eulerian form of the continuity equation is used. The general form of this continuity equation is:

$$\frac{\partial n}{\partial t} = -\nabla \cdot \mathrm{F} + P - L \qquad (1)$$

$\frac{\partial n}{\partial t}$is the partial derivative of the change in concentration with respect to the change in time and is in the units of molecules*cm^3/second. $\nabla \cdot$Fis the flux divergence transport in and out of the box, P is the combined rate of chemical production and emissions and L is the chemical loss and deposition. The CTM solves this equation numerically, solving for the concentration of a species at a particular time n(X, t_0 + Δt) when the initial conditions n(X,t_o) are known. The flux divergence is separated into turbulence and advection. Parameterizations are then used for to allow for a time averaged turbulent flux. The P and L variables are combined so that now there are three terms, advection, turbulence, and chemistry. Each of these terms is integrated separately. Through discretization of the spatial domain over a grid and by using the above approximations, a numerical solution is achieved.

1.2.3 Inverse Modeling

A chemical transport model solves for the fate of a chemical species, such as NO_2, given an emissions inventory and information that includes meteorology, chemical rate constants, and dry and wet deposition rates. This is referred to as a forward modeling. A simple way to consider this is that the species concentration is a function of the emissions.

In inverse modeling, observations of a chemical species are used to determine the initial conditions or parameters, such as emissions. The following equation applies to the forward model:

$$y = f(x) + \varepsilon \qquad (2)$$

where x refers to emissions and y is the species concentration. The inverse model seeks to solve for x given y. Two approaches for inverse modeling, the mass balance approach and the 4DVAR approach, shall be discussed in the next two subsections.

1.2.4 The Mass Balance Approach

A top-down inference of NO_x emissions is made from the observed tropospheric NO_2 column concentration (Ω_r) using mass balance following Leue et al. (2001). In addition to the observed NO_2 columns, which are in the units of molecules/cm^2, information about the lifetime of NO_x (τ_{NOx}) and the ratio of tropospheric NO_x to NO_2 columns is needed. This information is determined using a chemical transport model. The equation for top-down NO_x emissions (E_t), for each observation of NO_2 is as follows:

$$E_t = \alpha \Omega_r \tag{3}$$

where:

$$\alpha = \frac{\Omega_{NOx}/\Omega_{NO2}}{\tau_{NOx}} \tag{4}$$

The lifetime of NO_x is equal to the columns of NO_x divided by the sinks of NO_x. However, invoking a steady-state assumption for NO_x, the sinks are equal to the sources of NO_x. The sources of NO_x are emissions, chemical production, and transport. Neglecting transport and accounting for the fact that all the chemical processes are implicitly solved for in the model simplifies alpha to:

$$\alpha = \frac{E_a}{\Omega_a} \tag{5}$$

Where the subscript *a* denotes *a priori*, or derived from the model.

The top-down and bottom up emissions estimates are then combined following Martin et al. (2003). Using maximum likelihood and assuming a lognormal distribution of uncertainties in the top-down and bottom-up emissions, the *a posteriori* emissions estimate, *E*, becomes:

$$\ln E = \frac{(\ln E_t)(\ln \varepsilon_a)^2 + (\ln E_a)(\ln \varepsilon_t)^2}{(\ln \varepsilon_a)^2 + (\ln \varepsilon_t)^2} \tag{6}$$

Where ε_a and ε_t are the uncertainties in the bottom-up and top-down emissions, respectively.

1.2.5 The 4DVAR (adjoint) approach

The 4DVAR approach is based on Bayes' theorem, which states that:

$$P(x \mid y) = \frac{P(y \mid x)\,P(x)}{P(y)} \tag{7}$$

$P(x)$ and $P(y)$are the probability density functions (pdf) of vectors x and y. $P(y \mid x)$is the probability density of finding y given x and $P(x \mid y)$is the probability of finding x given y. If $P(x)$ is the pdf for *a priori* emissions derived from bottom- up sources, and $P(y \mid x)$ is the pdf for the observations obtained from the true emissions, then $P(x \mid y)$ is the pdf for the *a posteriori* emissions. $P(y)$is a normalizing factor.

The 4DVAR approach seeks to minimize a cost function derived from Bayes' theorem. This cost function accounts for the difference in simulated and observed NO_2, as well as the difference between *a priori,* and optimized emissions. The emissions are adjusted via use of linear scaling factors so that:

$$E^i = pE \tag{8}$$

whereE^i denotes the optimized emissions, p is the scaling factor and E is the initial emissions. The following cost function is used (*Henze*, 2007):

$$J = \frac{1}{2}\sum_{c\in\Omega}(c - c_{obs})^T S_{obs}^{-1}\,(c - c_{obs}) + \frac{1}{2}\gamma_r(p - p_a)^T S_p^{-1}(p - p_a) \tag{9}$$

In this cost function, c refers to the modeled column, c_{obs} are the columns derived from the observations, S_{obs} is the error covariance matrix for the observations, p_a are the *a priori* emissions scaling factors, p are the optimized emissions scaling factors, S_p is the error covariance matrix of the scaling factors and γ_r is a regularization parameter. The regularization parameter allows weighting of the cost function towards observations or emissions. Ω is the domain, in both time and space. The variables c and c_{obs} are vectors of observations the length of the entire domain. If m is the length of the vector, then m is equal to the product of the number of grid boxes for latitude, number of grid boxes for the longitude, and the number of time-steps. The corresponding vector containing the error variances of the observations would compose the diagonal of the error covariance matrix. The off-diagonal values in the error covariance matrix represent the error covariance between observations.

Following (Henze, 2009), the forward model calculates the concentration of NO_2, c, at any later time (N) as a function of the initial concentration and emissions (p)

$$c^N = F(c^0, p) \tag{10}$$

Looking at the function from a time step of n to $n+1$ the function can be written as:

$$c^{n+1} = F(c^n, p) \tag{11}$$

We assume that emissions are independent of the time index. The change in concentration from time n to time $n+1$ can be expressed as $\frac{\partial c^{n+1}}{\partial c^{n}}$. The sensitivity of the concentration at time $n+1$ to emissions, $\partial c^{n+1}/\partial p$ would be expressed by the Jacobian K and can be calculated using the chain rule.

$$K = \frac{\partial c^{n+1}}{\partial p} = \frac{\partial c^{n+1}}{\partial c^{n}} \frac{\partial c^{n}}{\partial c^{n-1}} \cdots . \frac{\partial c^{1}}{\partial c^{0}} \frac{\partial c^{0}}{\partial p} \tag{12}$$

The cost function can now be written as:

$$J = \frac{1}{2} \sum_{c \in \Omega} (Kp - c_{obs})^T S_{obs}^{-1} (Kp - c_{obs}) + \frac{1}{2} \gamma_r (p - p_a)^T S_p^{-1} (p - p_a) \tag{13}$$

and the gradient of the cost function at each point within the domain can be written as:

$$\nabla_p J(p) = S_{obs}^{-1} K (Kp - c_{obs}) + \gamma_r S_p^{-1} (p - p_a) \tag{14}$$

The adjoint method minimizes the cost function numerically by starting with an initial guess for the scaling factors ($p=p_a$). The CTM is run forward and then propagates information backwards. During the backwards propagation the cost function and its gradients are then calculated. The gradients are then fed into a steepest descent algorithm which then produces optimized scaling factors. This process continues until a minimum for the cost function is achieved. Figure 1.2 shows an example of an adjoint run where the cost function has converged.

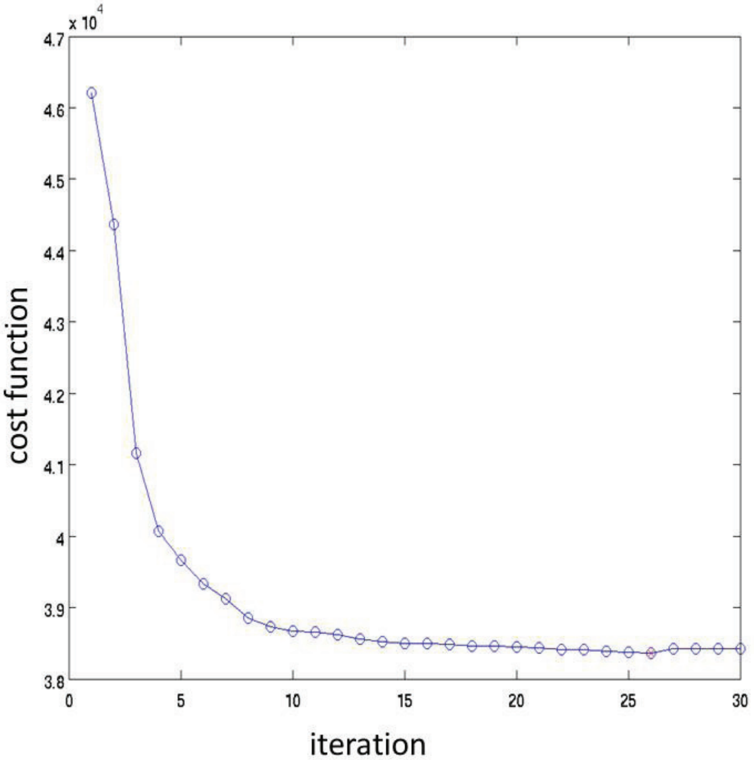

Figure 1.2: Cost functions derived at each iteration of a 4DVAR inversion. A minimum is achieved after26 iterations.

1.2.6 Comparison of Methods

Palmer et al.(2003) defined smearing as the horizontal displacement of the observed chemical species due to transport. The mass balance approach assumes transport of NO_x to be a negligible source of error, due to its short lifetime. However, Turner et al*.* (2012) showed the contribution of non-local sources of NO_2 to the column. The 4DVAR method takes into account spatial feedbacks, and should therefore be able to resolve smearing.

The 4DVAR method assimilates observations while the mass balance approach averages observations over time. Assimilating observations into the cost function allows solving for the spatial and temporal feedbacks. An assimilated mass balance can be used, such as the one performed by Zhao and Wang (2008), and would allow for the temporal feedbacks, but would take considerably more time than the mass balance approach that relies on averaging observations.

The errors are handled differently in the approaches. While both methods use the bottom-up and observational errors, the mass balance approach allows error in the modeled columns. The adjoint method assumes that the model columns are a perfect representation of emissions. Additionally, with the mass balance approach the errors for the same area over time are added in quadrature and then normalized by the number of observations. The 4DVAR approach relies on an error covariance matrix.

1.3 Derivation of Observations

The following section describes how the observations were derived from the satellite instruments.

1.3.1 Description of Satellite Instruments

SCIAMACHY (SCanning Imaging Absorption spectrometer for Atmospheric ChartographY), launched in 2002 aboard the Envisat satellite, measures direct and backscattered radiation at a wavelength range of 240-2380 nm (*Bovensmann et al.*, 1999). It alternately views the earth from a nadir (downward) or limbic (sideways) viewing geometry. The spatial resolution is 30-60km and global coverage is achieved, in the absence of clouds, every 6 days. For this study, NO_2 concentrations were retrieved as tropospheric columns.

The Global Ozone Monitoring Experiment-2 (GOME-2), aboard the MetOP satellite is a nadir viewing instrument that contains two spectrometers. GOME-2 covers a wavelength range of 240-790nm. The spatial resolution is 40-80km and global coverage is achieved in 1 day.

1.3.2 Retrieval Algorithm

The retrieval consists of several steps, following Chance (1998) and Martin et al., (2002). First, a spectral fitting using a reference spectrum (*Bogumil et al*., 2003), is fit to the backscattered radiance observed from SCIAMACHY at the wavelength region of 429-452nm (*Martin et al.*, 2006). This produces a slant columns density. It is called a slant column because of the geometry between the earth, sun, and satellite. It is a total column because it contains NO_2 concentrations for the entire atmosphere. This column also reflects the effects of atmospheric scattering on SCIAMACHY's vertically resolved sensitivity.

The next step of the retrieval is subtraction of the stratospheric column. The NO_2 concentrations over the central Pacific are assumed to be primarily stratospheric given the lack of sources in the area. Then the corresponding columns are subtracted for a given latitude and month. The small amounts of tropospheric NO_2 in the central Pacific are then corrected for using a chemical transport model (CTM) simulation (*Martin et al*., 2006). The error from the spectral fit and the stratospheric correction is estimated at $1X10^{15}$ molecules/cm^2 (*Martin et al*., 2004).

An Air Mass Factor (AMF) is then applied to the tropospheric slant columns to obtain the vertical tropospheric columns as follows:

$$\Omega_V = \frac{\Omega_S}{AMF} \tag{15}$$

where $\Omega_S$and Ω_V denote slant and vertical column. The Air Mass Factor formulation is based on Palmer et al., (2001) is as follows:

$$AMF = AMF_G \int_0^{\infty} w(z)s(z)dz \tag{16}$$

The Geometric AMF (AMF_G) solves for the geometry of the sun, earth, and satellite as a function of the solar zenith angle and the satellite viewing angle. The scattering weight (w) is the SCIAMACHY's sensitivity to NO_2 as a function of altitude and is determined using the Linearized Discrete Ordinate Radiative Transfer model (LIDORT), (*Spurr*, 2002). The shape factor (s) refers to the relative vertical distribution of NO_2 concentrations in the troposphere. Monthly mean shape profiles from 2006 were provided from CTM simulations.

The retrieval algorithm also takes into account surface reflectivity, aerosols, and cloud fraction. Monthly surface reflectivity fields are taken from Kleipool et. al (2008). Monthly local aerosol profiles from a CTM are used to correct for the extinction by aerosols (*Martin et al*., 2003). The retrieval has an inability to distinguish clouds from bright surfaces, such as snow. The Fast Retrieval Scheme for Cloud Observations (FRESCO+) algorithm is used to determine the fraction of each scenes in which clouds are present (*Wang et al*, 2008). This algorithm relies on the O_2 A-band to distinguish clouds and cloud top pressure.

This retrieval algorithm has been validated using *in situ* measurements taken from airplanes, as described in Martin et al. (2006). The typical uncertainty for each measurement has been estimated as 40% from the AMF formulation plus $1x10^{15}$ molecules/cm^2 from the spectral fitting and stratospheric subtraction (*Martin et. al*, 2006). Figure 1.3 shows the air mass factor and vertical tropospheric NO_2 columns for November, 2006.

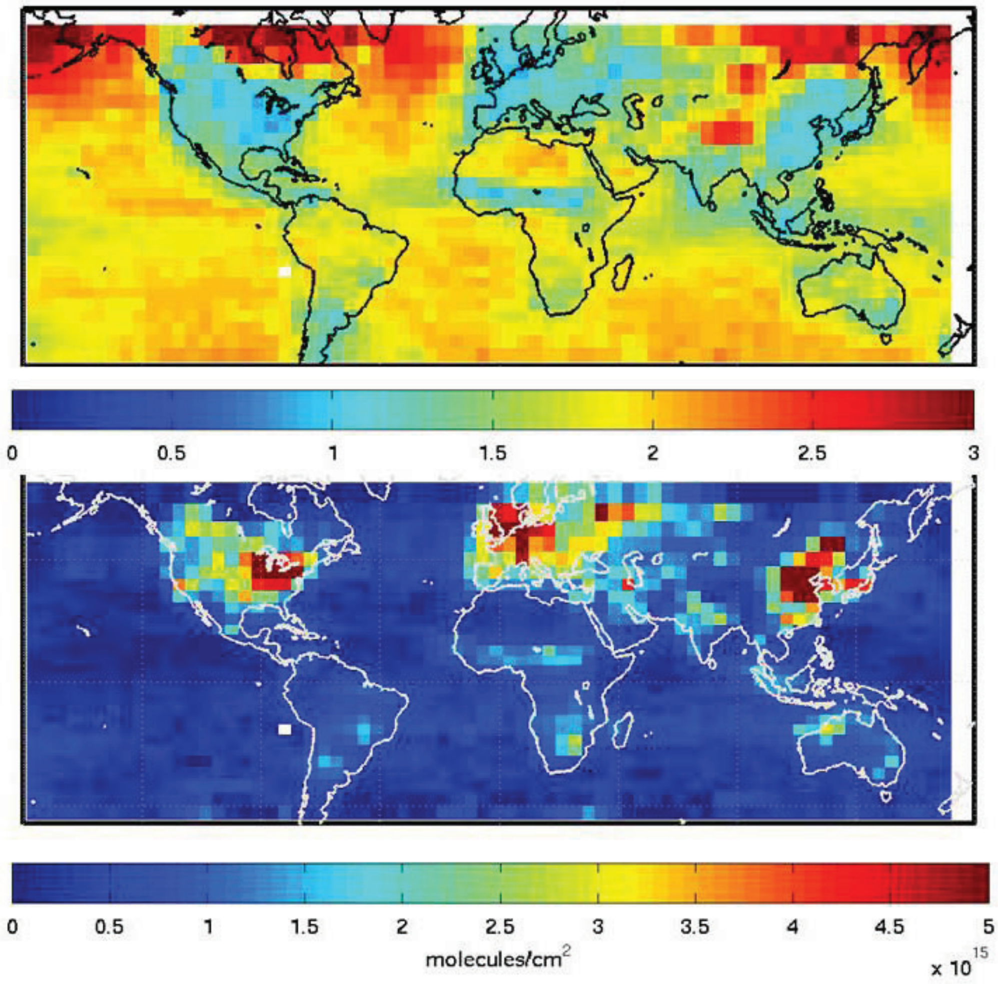

Figure 1.3:Air mass factor (top) and vertical tropospheric NO_2 columns (bottom) for November, 2006 derived from SCIAMACHY and gridded to a 4x5° resolution.

Chapter 2 Modeling Tools

The following subsections describe the chemical transport model, its adjoint, and the emissions inventory that have been used.

2.1 GEOS-Chem Chemical Transport Model

The GEOS-Chem Chemical Transport Model is used to determine the *a priori* emissions and the vertical distribution of NO_2 concentrations in the mass balance and for the forward run of the 4DVar method. The model uses assimilated meteorological fields from NASA's Goddard Earth Observing System (GEOS-5) and includes a detailed simulation of ozone-NO_x-Hydrocarbon chemistry as well as aerosols and their precursors (*Bey et al.*, 2001; *Park et al.*, 2004). The gaseous and aerosol simulations are coupled through the formation of sulfate and nitrate, the HNO_3/NO_3^- partitioning of inorganic nitrate, and heterogeneous chemistry including uptake of N_2O_5 on aerosols (*Evans and Jacob*, 2005). Photolysis rates in the troposphere are calculated using the Fast–J algorithm, which accounts for Mie scattering of clouds (*Wild, et al.,* 2000). The chemical mass balance equations in the troposphere are integrated every hour. The meteorological data from GEOS-5 has a 6 hour temporal resolution. This study uses version 8-01-01 of the model. Vertically the model version used has 47 vertical levels up to 0.01hPa and horizontally the resolution is either 4x5° or 2x2.5° latitude by longitude. In an online simulation, it solves for the fate of about 120 chemical species and transports 43 tracers. The NO_x chemistry has been extensively validated (*Martin et al*., 2002, *Martin et al*., 2006, *Hudman, et al*. 2007, *Lamsal et al*., 2008, 2010). Figure 2.1 shows the surface NO_x emissions for November 15-22 and July 15-22, 2006 as derived from GEOS-Chem.

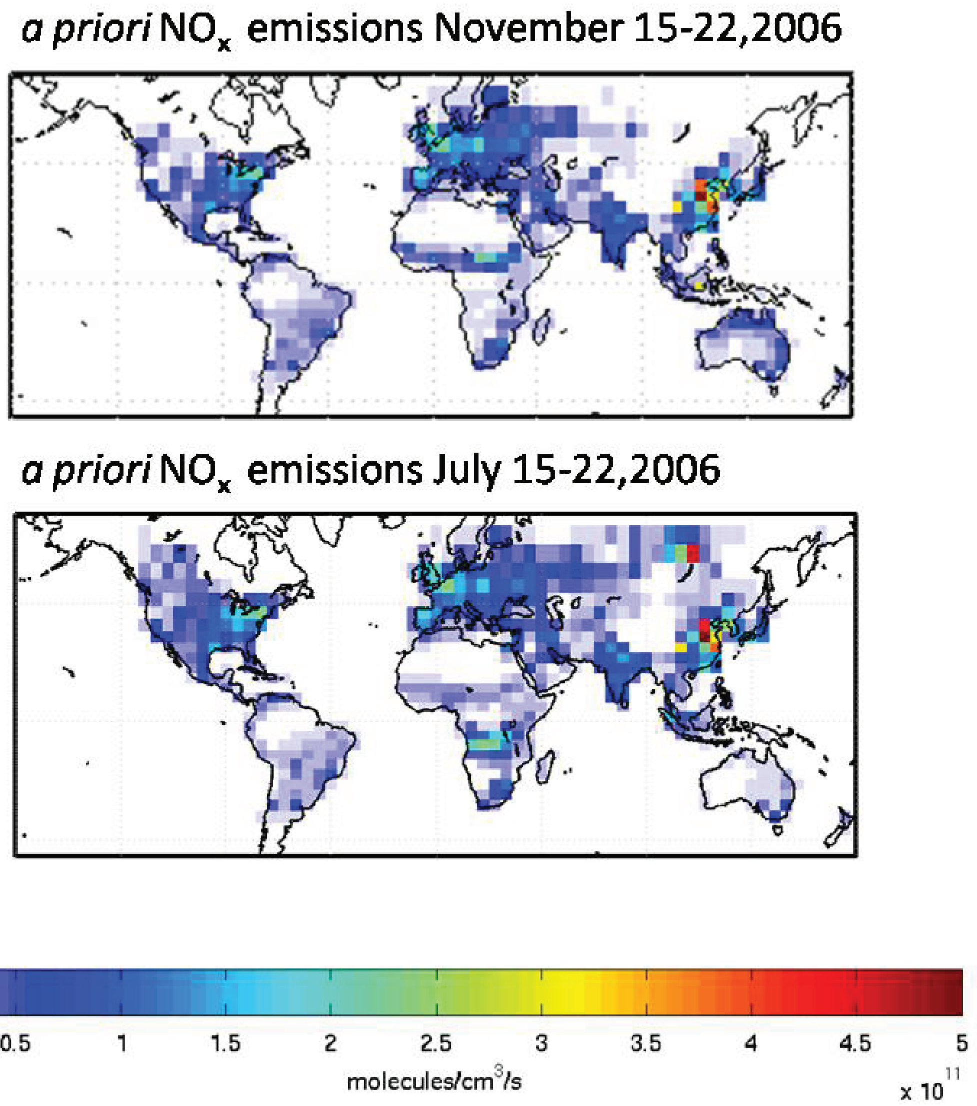

Figure 2.1: *A priori* NO_x emissions for November 15-22, 2006 and July 15-22, 2006 as derived from the GEOS-Chem chemical transport model.

2.2 The GEOS-Chem Adjoint

The GEOS-Chem Adjoint derives the necessary gradients using equations from the forward model code (*Henze*, 2007). After the forward model is run, the adjoint runs the code backward and calculates the cost function and adjoint forcings. The Tangent and Adjoint Model Complier (TAMC, *Giering and Kaminski*, 1998), and the Kinetic Pre-processor (*Sandu et al.,* 2003, *Damian et al*.,2002, *Daescu et al.*, 2003) are used for constructing the adjoint of chemical mechanisms (*Henze*, 2007). At the end of the iterations, the gradients are fed into the quasi-Newton L-BFGS-B optimization routine (*Byrd et al*., 1995; *Zhu et al*,. 1994) and new scaling factors are determined. This process is repeated in subsequent iterations until a minimum of the cost function is achieved. A full description of the adjoint can be found in Henze (2007). Figure 2.2 shows the process that occurs in the adjoint model. Figure 2.3 shows an example of how the linear scaling factors and gradients change from the first to the final iteration.

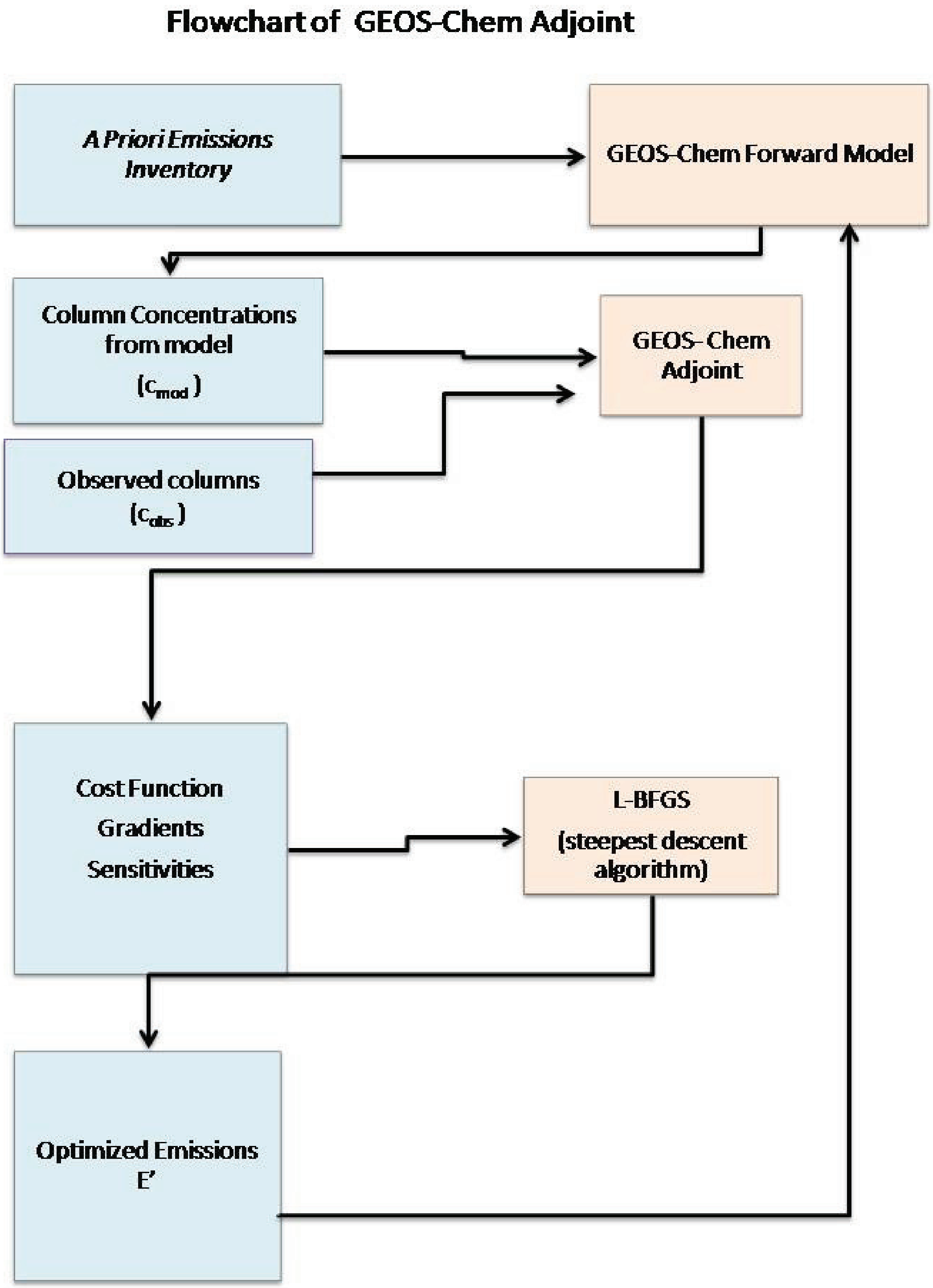

Figure 2.2: A schematic showing the GEOS-Chem adjoint process .

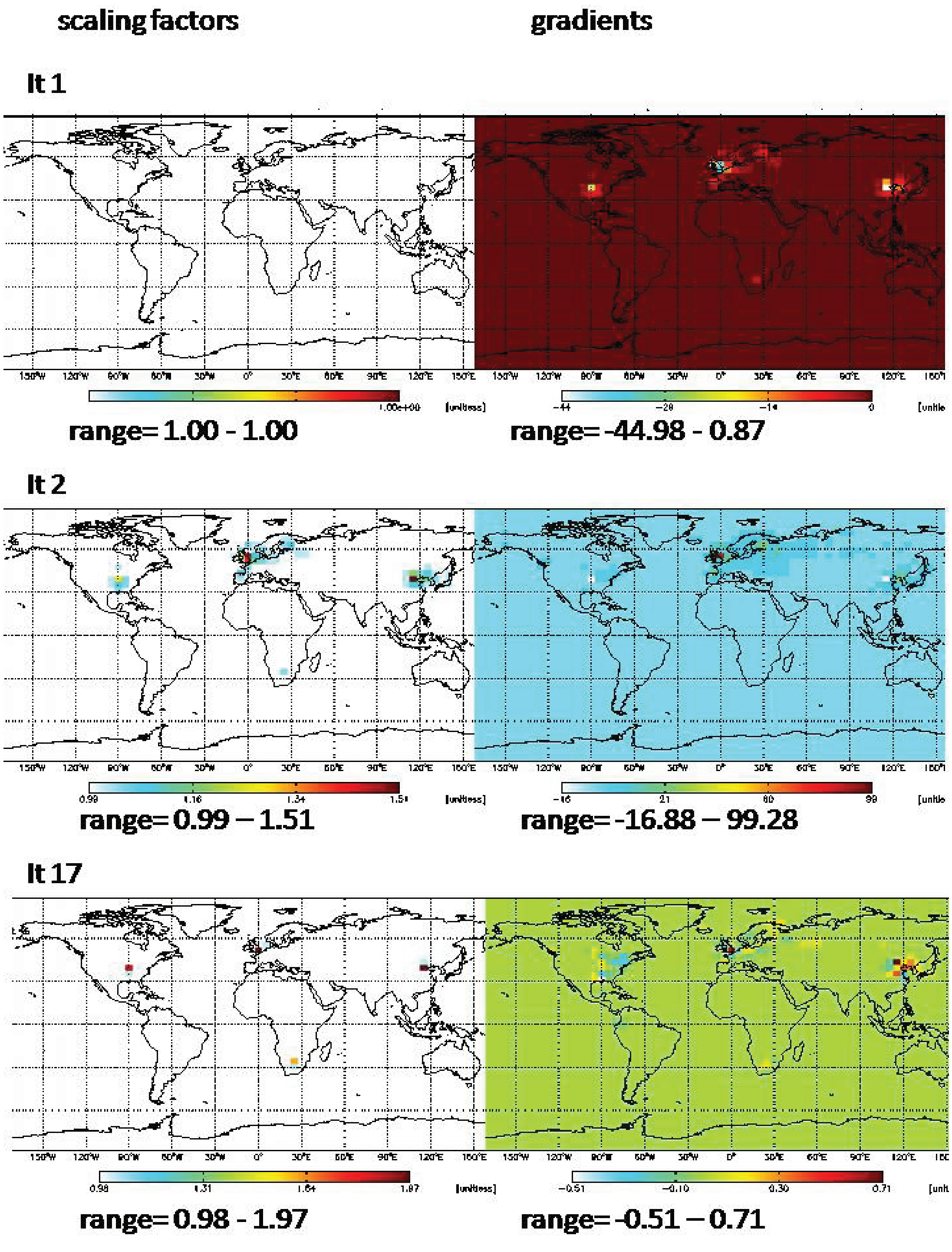

Figure 2.3: example of scaling factors (left) and gradients (right) calculated at iteration 1 (top), 2 (middle), and 17(bottom) of the GEOS-Chemadjoint.

2.3 Emissions Inventory

The global anthropogenic NO_x emissions inventory is from EDGAR (Olivier, et al., 2001). Over the following regions the EDGAR emissions inventory is overwritten by regional inventories: EPA/NEI99 for the US, EMEP for Europe, Streets et. al (2006) for southeast Asia, BRAVO for Mexico, and CAC for Canada. Biomass burning emissions are from GFED. The soil NO_x emissions inventory is based on the work by Yeinger and Levy (1995) and Wang (1998). The global biofuel inventory is from Yeinger and Logan (2003) with overwrites over North America from EPA/NEI99 and over by the Streets et. al (2006) inventory over China and Southeast Asia. Following Hudman, *et al. (2007)*, the midlatitude lightning source of NO_x is estimated at 1.6 Tg N yr^{-1}. Figure 2.1 shows the *a priori* NO_x emissions derived from GEOS-Chem for November and July of 2006.

Chapter 3 Inversion of Observations

This chapter discusses the methods and results from assimilating observations.

3.1 Four-point perturbation pseudo- observations tests

A “true” NO_x emissions dataset and pseudo-observations were created using GEOS-Chem at a 4°x5° and 2°x2.5° resolution. The standard model was used, but for simplicity the anthropogenic NO_x emissions came only from the global EDGAR inventory, without the regional overwrites. The surface NO_x emissions in grid boxes over the Ohio Valley, London, Beijing, and Johannesburg were doubled in this inventory. These areas all have large emissions of NO_x. Emission datasets were created for the time period of Nov 15-22 and July 15-22 with a 15 day spin-up. The forward model was run to determine the NO_2 column concentrations. Synthetic observations of NO_2 for these time periods were archived for every hour. To recover the “true” emissions using both the adjoint and mass balance inversion, we used the standard model of GEOS-Chem, without the regional overwrites or perturbation of emissions in the 4 grid boxes. Figure 3.1 shows the “true” emissions for November and July. These months were chosen to examine the effect of seasonality on the inversions. Satellite observations are often excluded over snow, so November was chosen instead of January to reduce occurrences of snow.

Tests were run to look at the effects of seasonality, resolution, number of observations, and the addition of random error to observations. An iterative mass balance inversion was also explored, where we performed the mass balance inversion several times using the *a posteriori* emissions from the previous iteration as the *a priori* emissions for the subsequent run, following Ghude et al. (2013). The *a posteriori* emissions derived (E_a) from each experiment were recovered and the normalized mean error (NME) bias was calculated using true emissions (E_T) and the following equation (*Boylan and Russell*, 2006):

$$NME = \sum_{i=1}^{N} \frac{|E_T - E_a|}{\sum_{i=1}^{N} E_a} \tag{17}$$

The results from the GEOS-Chem simulation used in the mass balance calculation took about 1 hour to produce at a 4x5 resolution. Each result from the adjoint inversion took about 15-35 iterations at about 2 hours per iteration.

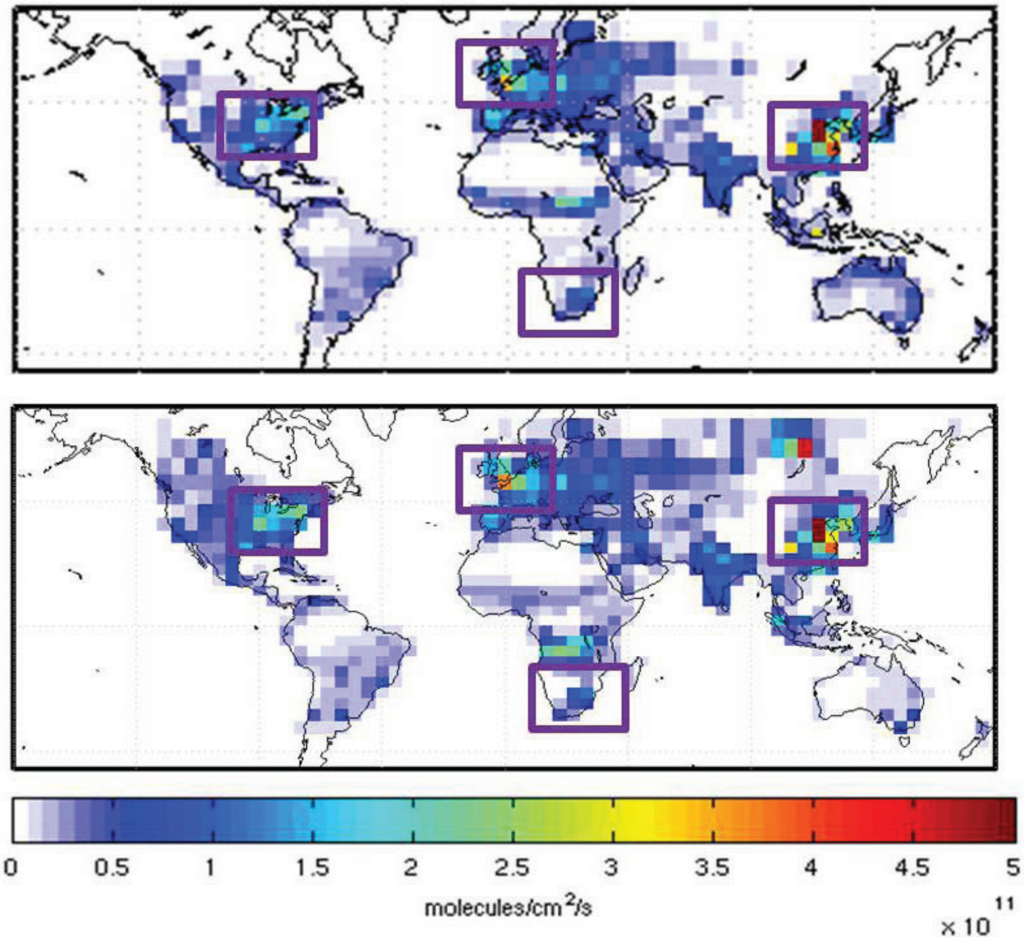

Figure 3.1 "True" Surface NO_x Emissions for November 15-21, 2006 (top) and July 15-21, 2006 (bottom). "True" Emissions refer to GEOS-Chem simulations where surface NO_x in pixels over London (51N, 0.1W), Beijing (40N, 116E), Johannesburg (26S, 28E), and the Ohio Valley (37N, 89W) have been doubled.

3.1.1 Error Specification

In both inversions the relative error in observations was assumed to be 30%. The uncertainties NO_x surface emissions were designated as follows: 50% for anthropogenic emissions, 300% for soil and biomass burning, and 200% for biofuel. The adjoint model assumes that the modeled NO_2 columns are perfect. The error in the ratio of modeled columns to *a priori* emissions was assumed to be 30%, based on previous studies (Martin, 2004). This value is incorporated into the mass balance inversion. However, for consistency, tests were run using the mass balance inversion where the model was treated as perfect.

The *a posteriori* inventory in the mass balance is obtained by using a weighted average between the top-down and bottom-up estimates. In the mass balance inversion, the errors are used to weight the *a posteriori* emissions towards the top- down or bottom up emissions. Figure 3.2 shows the difference between true emissions and bottom-up and top-down derived emissions for November 15-21. The top-down emissions derived from the satellite show evidence of smearing in the pixels adjacent to those where sources were perturbed. Assuming a perfect modeled column weighs the solution more towards the top- down inventory than an imperfect column.

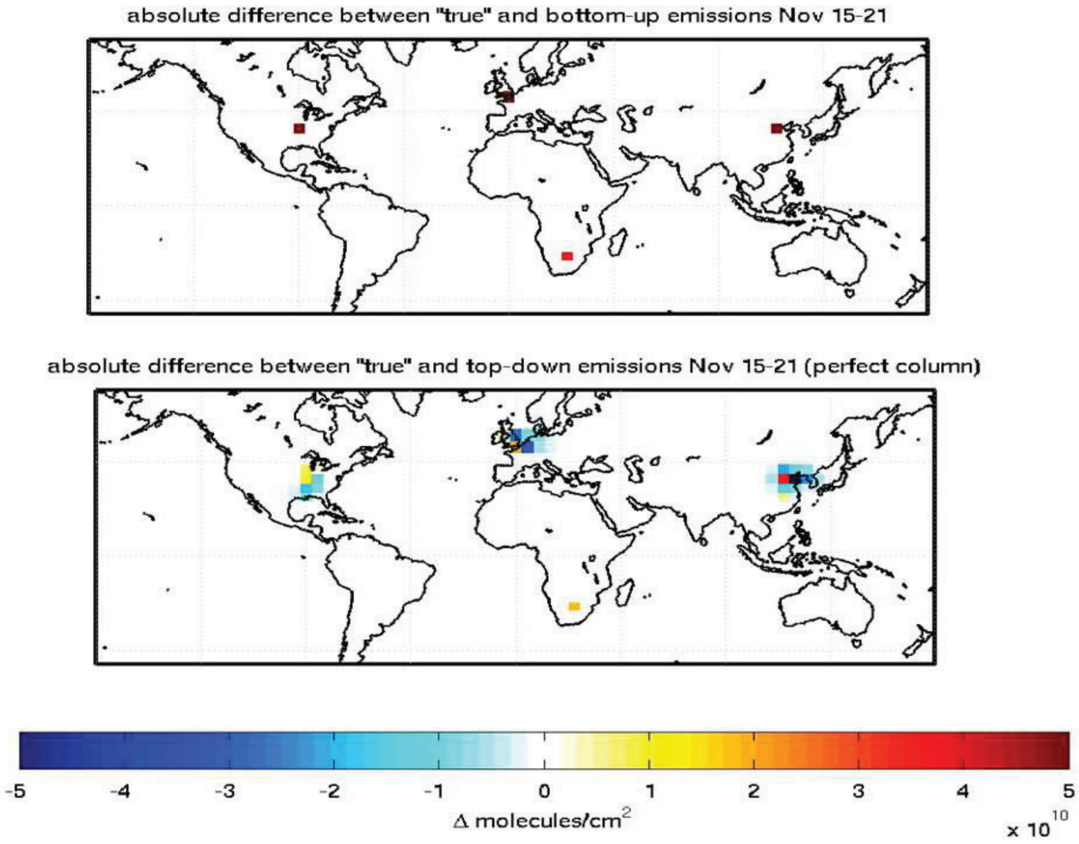

Figure 3.2: Absolute difference between “true” NO_x emissions and bottom- up emissions, true –minus bottom-up (top) and true minus top-down (bottom). “True” Emissions refer to GEOS-Chem simulations where surface NO_x in pixels over London, Beijing, the Ohio Valley, and Johannesburg have been doubled.

Figure 3.3 shows the normalized mean errors for cases in both November and July and at 4x5 and 2x2.5 resolution. When the errors in the top- down estimate are lower than the bottom- up, assuming the perfect forward model produces the best results. However, as in the November case (where NO_x lifetime is longer) and at 2x2.5 resolution (where advection distance is shorter), the bottom-up and top-down errors are similar regardless of whether the errors are assumed for the forward model.

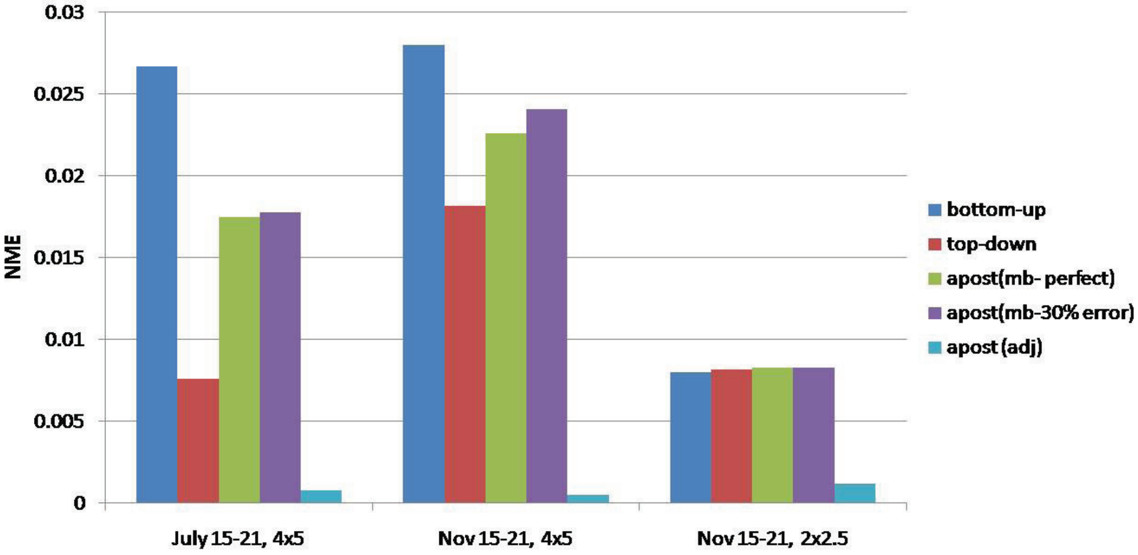

Figure 3.3: Normalized mean error for 4-point perturbation tests that invert pseudo-observations (every hour) of the given time period (556416 observations for 4x5 resolution and 2,201,472 observations for 2x2.5). The abbreviation apost refers to *a posteriori* emissions, mb-perfect to a mass balance inversion with the forward model treated as perfect, mb-30%error as the mass balance inversion where a 30% error in the forward model is assumed, and adj as the adjoint inversion.

3.1.2 Seasonality

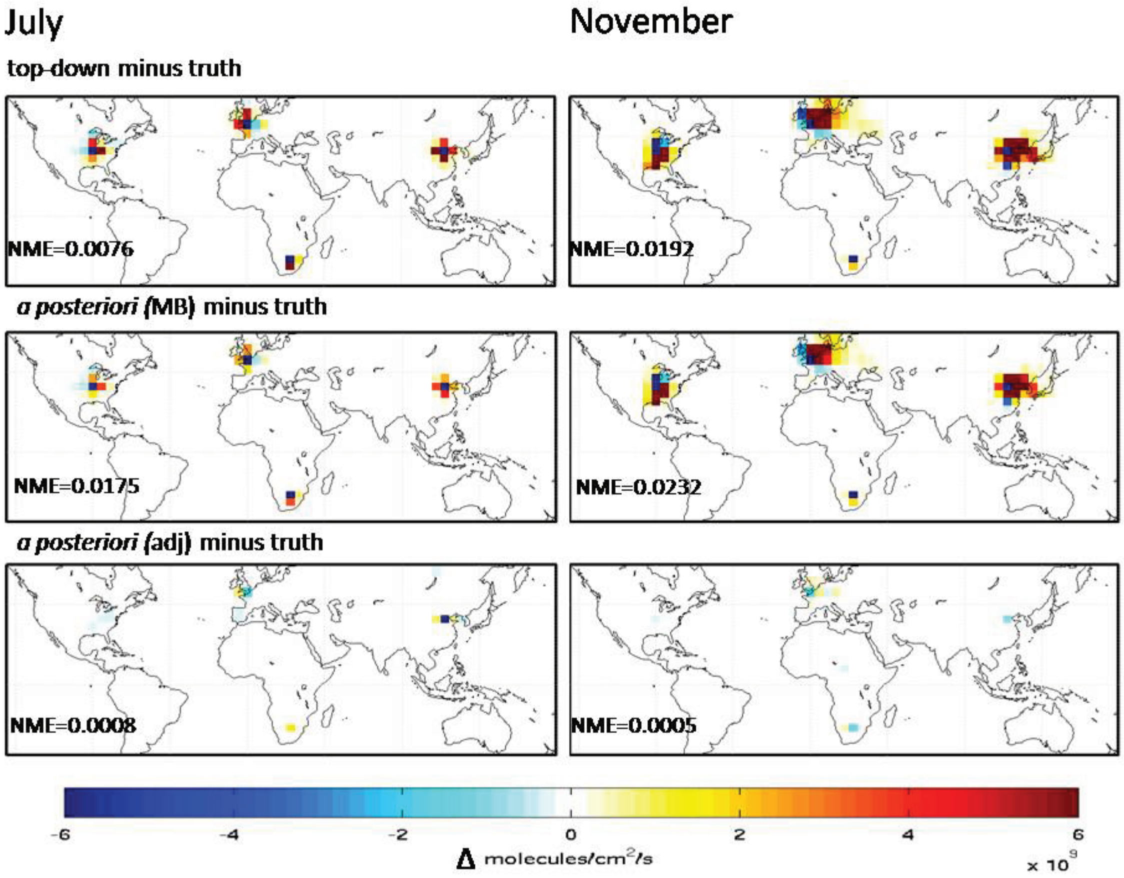

Figure 3.4: Absolute differences, at a 4x5 resolution, between “top-down” derived emissions and “truth” (top), Mass Balance Approach and “truth” (middle) and Absolute Difference between Adjoint Approach and “truth” (bottom) for July15-22, 2006 and January 15-22, 2006 . “True” Emissions refer to GEOS-Chem simulations where surface NO_x in pixels over London, Beijing, Johannesburg, and the Ohio Valley have been doubled. There are observations for every hour over every grid box. Observational error is assigned as 30% and forward model is considered perfect.

Figure 3.4 shows the difference in truth and recovered emissions using all pseudo observations generated for the time periods in July and November- 556,416 pseudo observations for each month. In both cases the adjoint inversion has lower error than the mass balance inversion by an order of magnitude. This is the case with both the top down derived emissions and the *a posteriori* mass balance estimates. In November, figure 3.4 shows that the spatial smearing is more evident in the Northern Hemisphere than for July. During summer months, the lifetime of NO_x is considerably shorter than the winter, where the lack of sunlight slows down the mechanism for NO_x loss. This longer lifetime allows for more transport of NO_x through advection. The errors in the adjoint are consistent throughout July and November, indicating that smearing is not likely the cause.

A key difference between both methods is that the values generated by the mass balance are consistently low in the perturbed pixels. Two possible explanations are nonlinearity in the NO_2/NO_x ratio or advection of nonlocal NOx. Martin *et al.* (2006) explored the NO_2 to NO_x ratio, or alpha value from the mass balance derivation. They found through sensitivity tests that, in several locations, the relationship between NO_2 and surface NO_x was relatively linear in GEOS-Chem simulations. Figure 3.5 shows this relationship in the 4 perturbed areas. The Ohio Valley has one outlying point which is not understood. Nonetheless, all areas demonstrate a linear relationship. Thus, nonlinearity can be ruled out as a source of bias in the 4 regions. The influence from of NO_x transport from adjacent regions seems likely.

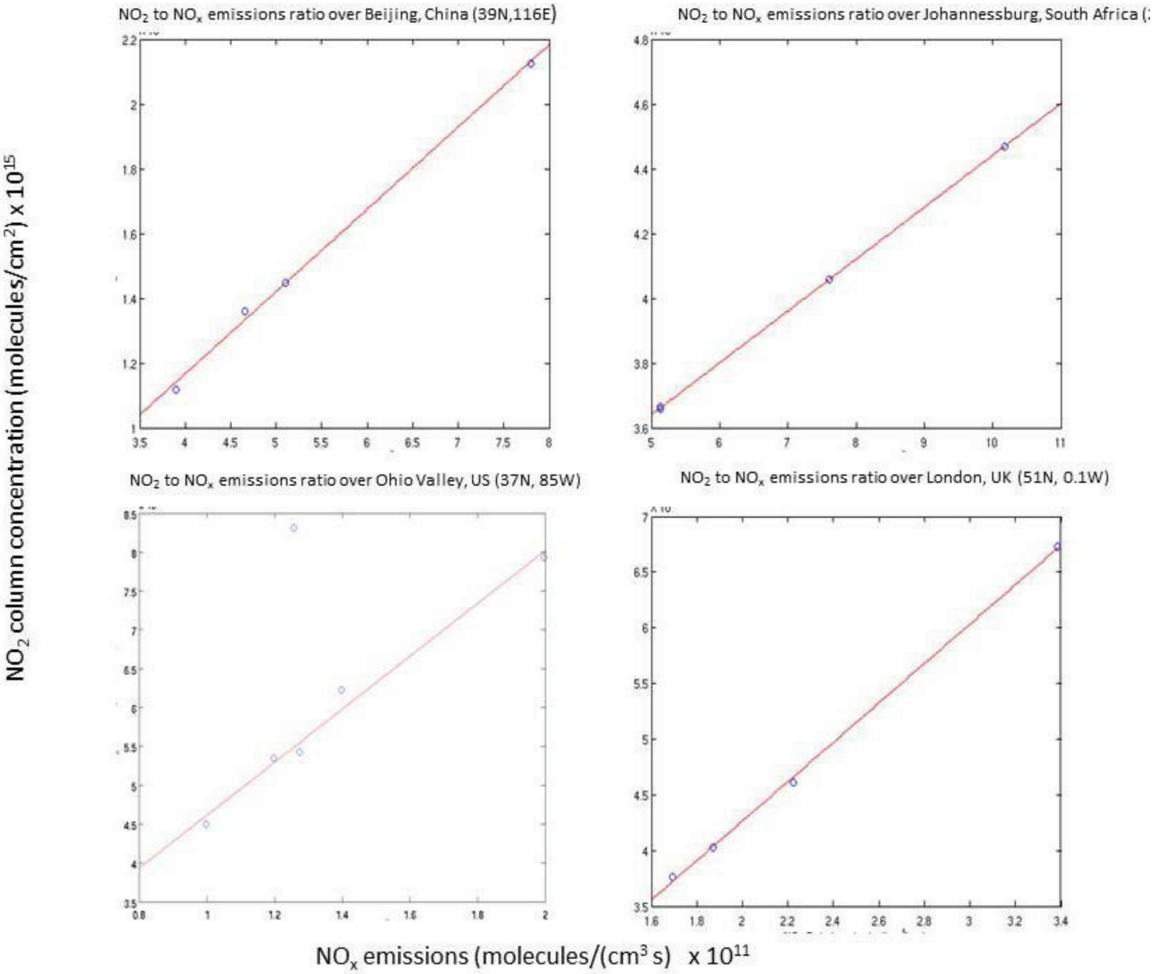

Figure 3.5: NO_2 columns versus NO_x emissions over four areas: Johannesburg(26S, 28E) , London(51N, 0W), the Ohio Valley(37N, 89W), and Beijing(40N,116E). Dots indicate the $NO_2$to NO_x ratios derived from different GEOS-Chem simulations for Nov 15-22, 2006.

A smaller perturbation in emissions of 30% in the four pixels was then explored. Figure 3.6 shows the results from a simulation where emissions at the four points were perturbed by 30%. The error in the mass balance is reduced by about a factor of three, yet the error in the adjoint inversion is similar to before. The smearing is still an issue in the mass balance inversion but not in the adjoint inversion. Again, November has a higher degree of smearing in the mass balance inversion.

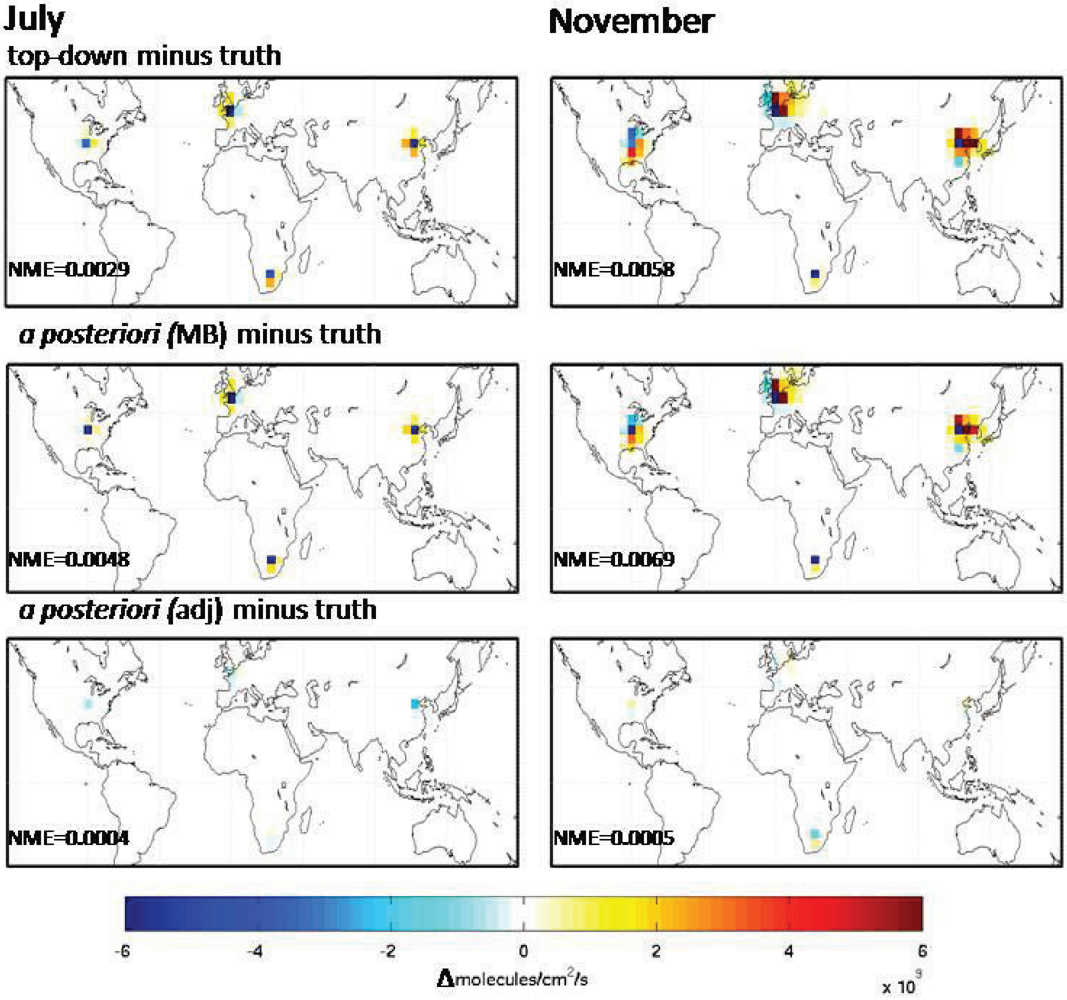

Figure 3.6: Absolute differences between "top-down" derived emissions and "truth" (top), Mass Balance Approach and "truth" (middle) and Absolute Difference between Adjoint Approach and "truth" (bottom). "True" Emissions refer to GEOS-Chem simulations where surface NO_x in pixels over London, Beijing, Johannesburg, and the Ohio Valley have been increased by 30%. There are observations for every hour over every grid box. Observational error is assigned as 30% and forward model is considered perfect.

3.1.3 Resolution

Figure 3.7 shows the absolute difference between the true emissions and the *a posteriori* emissions derived by the mass balance and adjoint inversions at a 2°x2.5° resolution. The error in the bottom-up emissions inventory is expected to be smaller at this resolution because 4 out of 13104 pixels were perturbed rather than 4 out of 3312. It is also expected that the pixel smearing would be higher at this resolution because the distance between each grid-box is half as much as in the 4x5 resolution. In the mass balance inversion the smearing is evident in the Northern hemisphere around the 4 perturbed points. The higher resolution also causes smearing to be evident in the Southern hemisphere, over Johannesburg. The emissions derived from the adjoint inversion begin to show smearing in the Northern hemisphere as well, but not to the same extent as the emissions derived from the mass balance inversion. The normalized mean error from the adjoint inversion increases with the higher resolution. This indicates that either the adjoint is less likely to resolve smearing at the higher resolution or that there are increased feedbacks from other sources such as chemistry and deposition at a higher resolution.

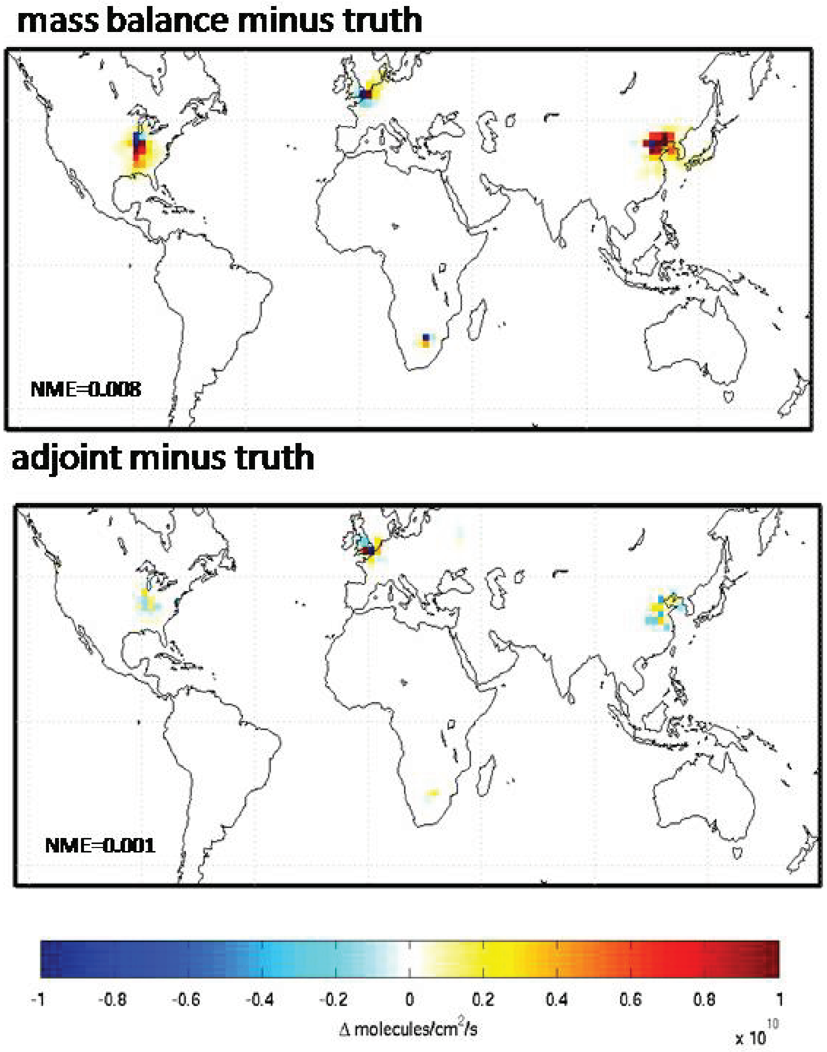

mass balance minus truth

adjoint minus truth

Figure 3.7: Absolute Difference between Mass Balance Approach and “truth” (top) and Absolute Difference between Adjoint Approach and “truth” (bottom) at a 2x2.5 resolution. “True” Emissions refer to GEOS-Chem simulations where surface NO_x in pixels over London, Beijing, Johannesburg, and the Ohio Valley have been doubled. There are observations for every hour over every grid box for November 15-21, 2006.

3.1.4 Number of Observations

When assimilating satellite data, it is unlikely to have hourly global observations. The observations are made during the satellite overpass which is usually once a day. At a 4°x 5° resolution that would be 3312 observations for cloud-free conditions. The mass balance inversion averages the data in each grid box over time. This will smooth some of the random error in observations. In this case, the synthetic observations are perfect, or without random error so the mass balance is relatively unaffected by the number of observations. Figure 3.8 shows that the error in the adjoint inversions decreases with increased observations. Although reducing the observations increases the normalized mean error in the adjoint inversion, Figure 3.8 shows that the error is still consistently lower than in the mass balance inversion. The adjoint inversion uses spatial feedback as well as temporal feedback so even if there is only one time-step of observations, there is still feedback from surrounding areas. Figure 3.9 shows that the adjoint method is less effective at resolving smearing when fewer observations are used because it receives less feedback from surrounding observations.

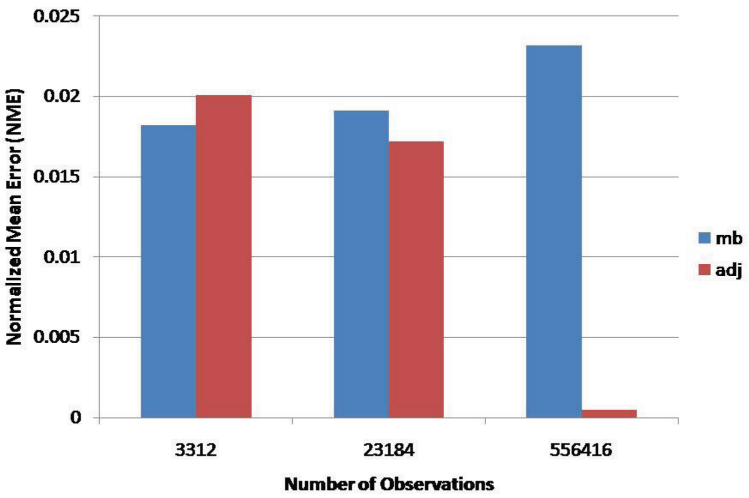

Figure 3.8: Normalized Mean Error (NME) versus number of assimilated observations for both methods at 4x5 resolution for November 15-21. In the mass balance approach, a perfect forward model is assumed to maintain consistency between methods.

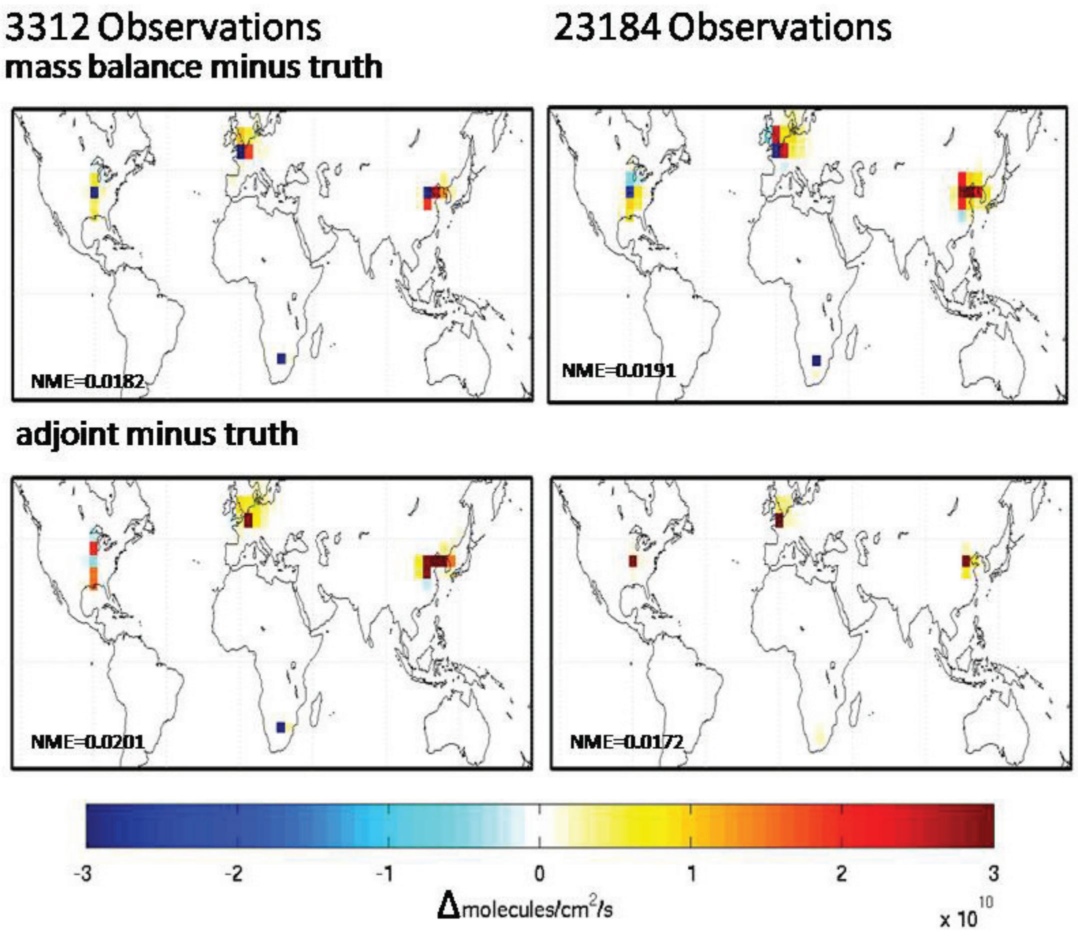

Figure 3.9: Absolute Difference between Mass Balance Approach and "truth" (top) and Absolute Difference between Adjoint Approach and "truth" (bottom). "True" Emissions refer to GEOS-Chem simulations where surface NO_x in pixels over London, Beijing, Johannesburg, and the Ohio Valley have been doubled. The observations in the left slides are for every pixel at 10am on November 21. The right slides use observations for 10 am, November 15-21.

3.1.5 Iterative Mass Balance

Using an iterative mass balance approach, Kuenen (2006) was able to reduce the difference between simulated and observed columns. The results lead to the conclusion that an iterative process compensated for the spatial smearing of NO_2 observations. However, Figure 3.10 shows that the iterative process does not resolve smearing. The process appears to move the recovered emissions more towards the “top-down” inventory, which actually exaggerated smearing in subsequent iterations. Because the “top-down” estimate is weighted more in this approach, the emissions at the 4 points move closer to “truth” until iteration 4, where they become greater than the true emissions.

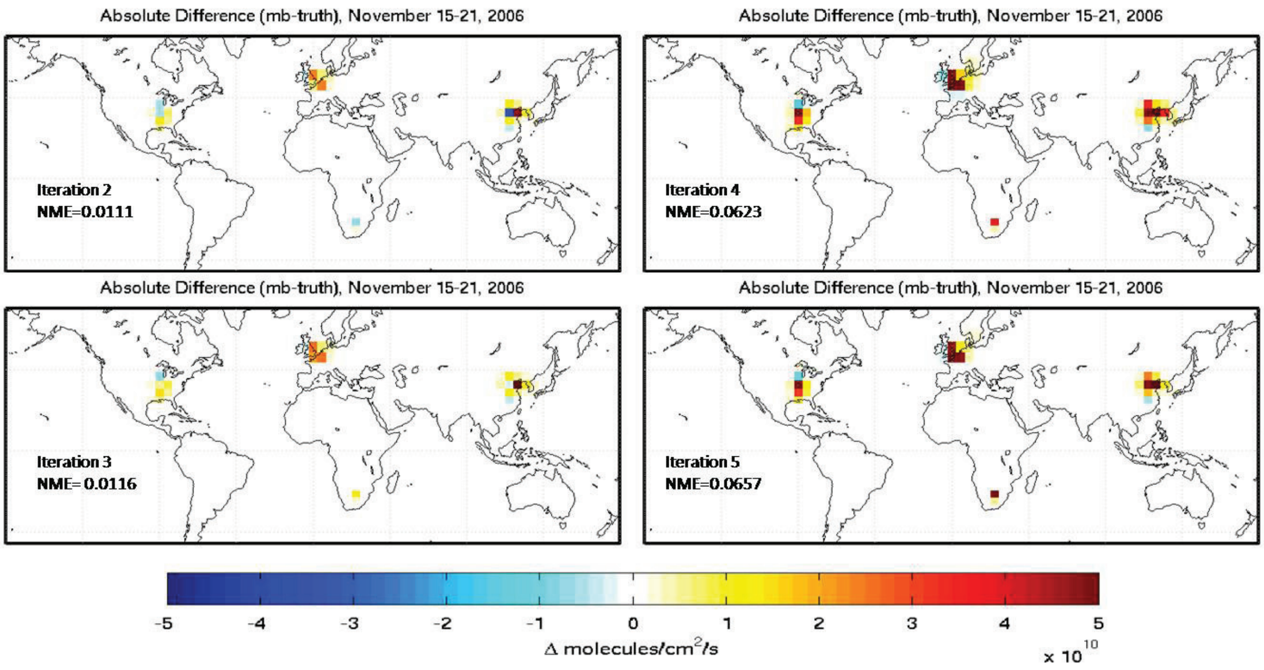

Figure 3.10: Absolute difference between true emissions and those recovered during iterative mass balance for November 15-21, 2006.). “True” Emissions refer to GEOS-Chem simulations where surface NO_x in pixels over London, Beijing, Johannesburg, and the Ohio Valley have been doubled. There are observations for every hour over every grid box. Observational error is assigned as 30% and forward model is considered perfect.

3.1.6 Adding Random Errors to Observations

The previous experiments all dealt with pseudo observations that were perfectly generated from the forward model. However, in reality, observations will include some degree of error. So another test was performed, adding uniform random error of up to 10% into the observations generated by the forward model.

A set of 23184 random numbers between uniformly distributed between 0.90 and 1.10 with a mean of 1 were generated. Observations from 10am for everyday of the simulation were used (23184 observations), with each observations being perturbed by multiplication by one of the random numbers. For consistency the forward model was treated as perfect in the mass balance inversion. Figure 3.11 shows the normalized mean error for these tests. The adjoint performed better than the mass balance inversions, but to a lesser extent than in the previous experiments. It was expected that neither inversion would improve the *a priori* since the observations now had a higher error than the modeled columns but the adjoint showed a slight improvement over the *a priori*. The same test was performed with 30% uniform random error and 50% uniform random error in the observations and in these cases the mass balance performed better than the adjoint. Figure 3.12 shows the absolute difference between the derived emissions and truth. Because the mass balance inversion averages all observations over the specific grid box for the entire time period, the random errors in the observations appear to be smoothed out better than in the adjoint inversion.

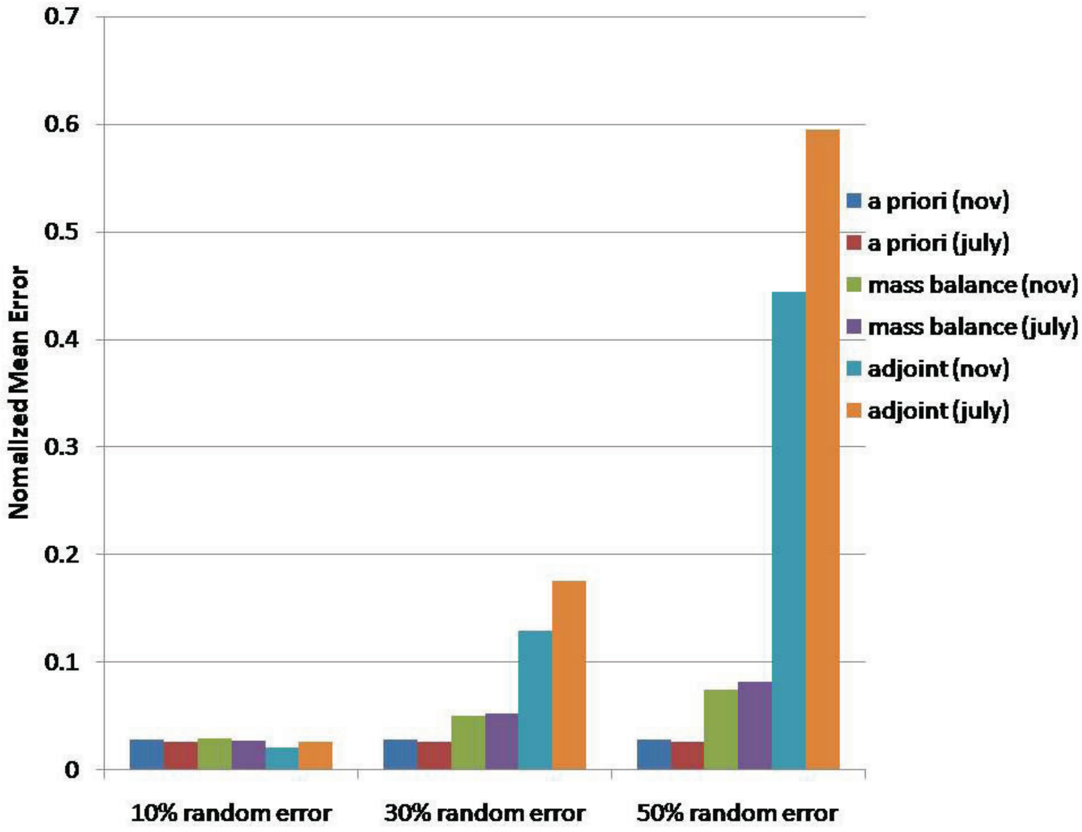

Figure 3.11: The Normalized mean error for the *a priori,* mass balance, and adjoint emission inventories for November 15-21 and July 15-21 when adding random noise to observations. Each simulation assimilated 23,184 observations at a 4x5 resolution (10am each day).

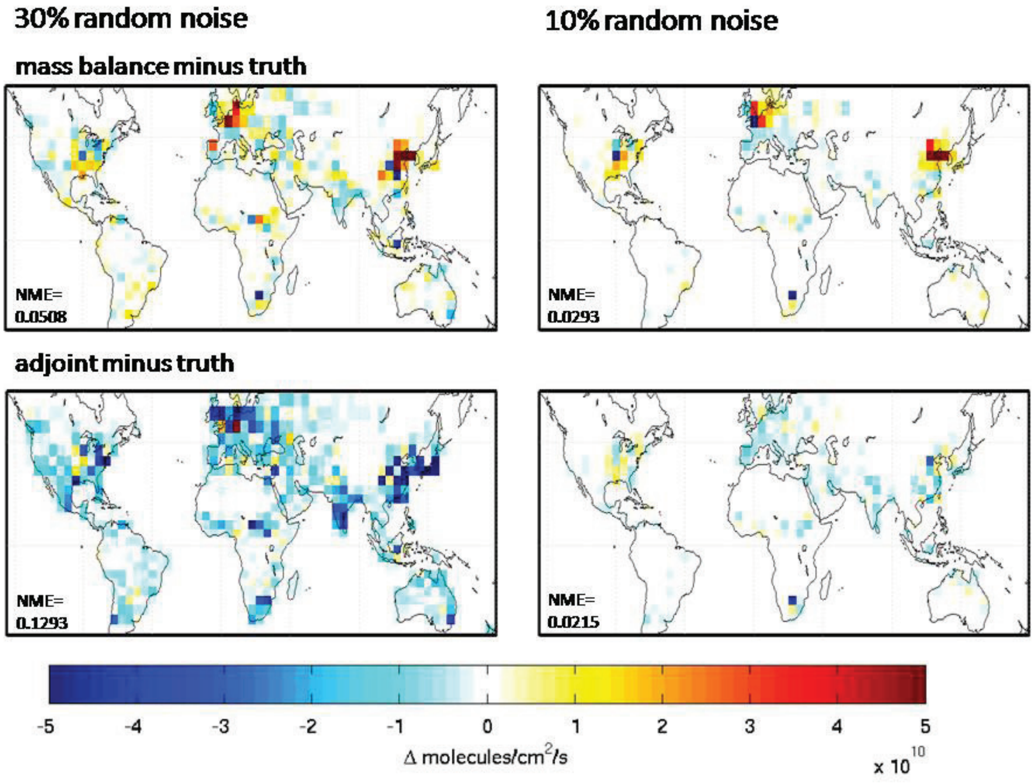

Figure 3.12: Absolute difference between true inventory and a posteriori inventories derived from the mass balance (top) and adjoint (bottom) approach. For November 15-21, 2006 In the true case emissions in pixels above the Ohio Valley, London, Beijing, and Johannesburg have been doubled. The observations are for 10am November 15-21 and have had random noises of up to 30% and 10% added in each case.

The error in emissions derived from the adjoint decreased as observations increased in previous experiments so the two inversions were tested further using the observations with up to 30% random error. The number of observations assimilated was varied as following for November: 2 weeks of 10 am assimilations (46,368 observations), 1 month of 10 am observations (99,360 observations), and 1 week of hourly observations (556,416). For July observations were assimilated for 1 month and 1 week. Figure 3.13 shows the errors derived from each method as a function of observations. For both July and November, the adjoint requires approximately 1 month of observations to outperform the mass balance.

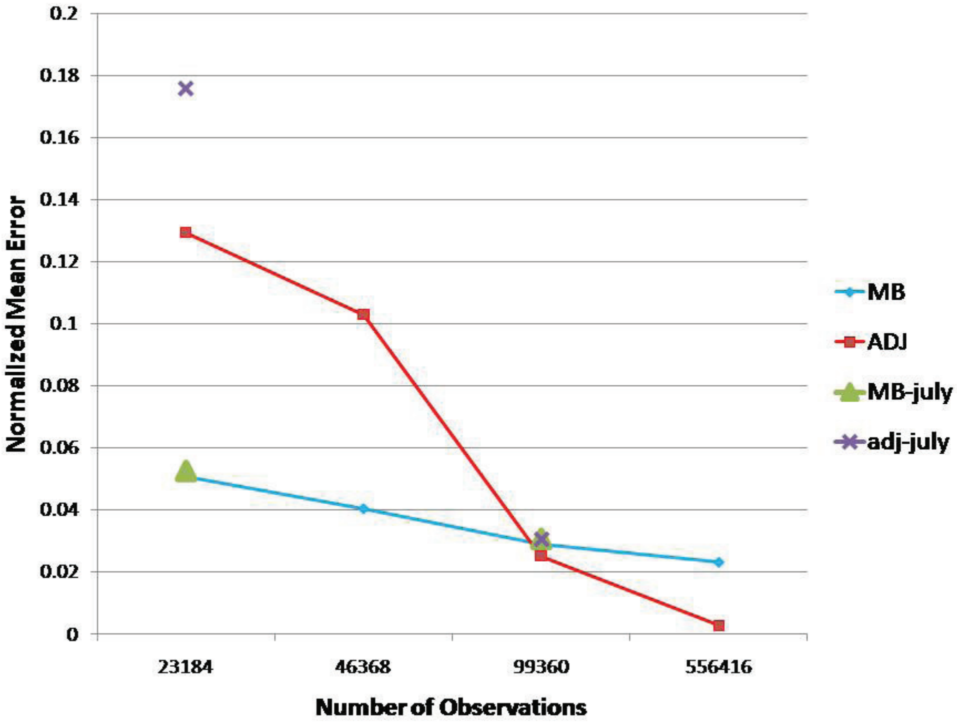

Figure 3.13: Normalized mean Error (NME) versus number of observations assimilated for November, 2006 and July 2006. Observations have random errors of up to 30% added.

3.1.7 Cloud filter

Clouds impair the satellite retrieval's ability to represent the NO_2 column accurately because they prevent solar radiation from reaching the surface. To reduce the effect of clouds onto the measurements, observations that contain 50% or more cloud coverage are eliminated from the data. Therefore, if measurements are made once a day for a 30 day period, there will be less than 30 observations in each pixel. Figure 3.14 shows the actual amount of observations that were assimilated from SCIAMACHY for November, 2006. 460,452 measurements were kept, but those that were in the same grid box at the same hour were averaged together. The result was a total of 22501 observations.

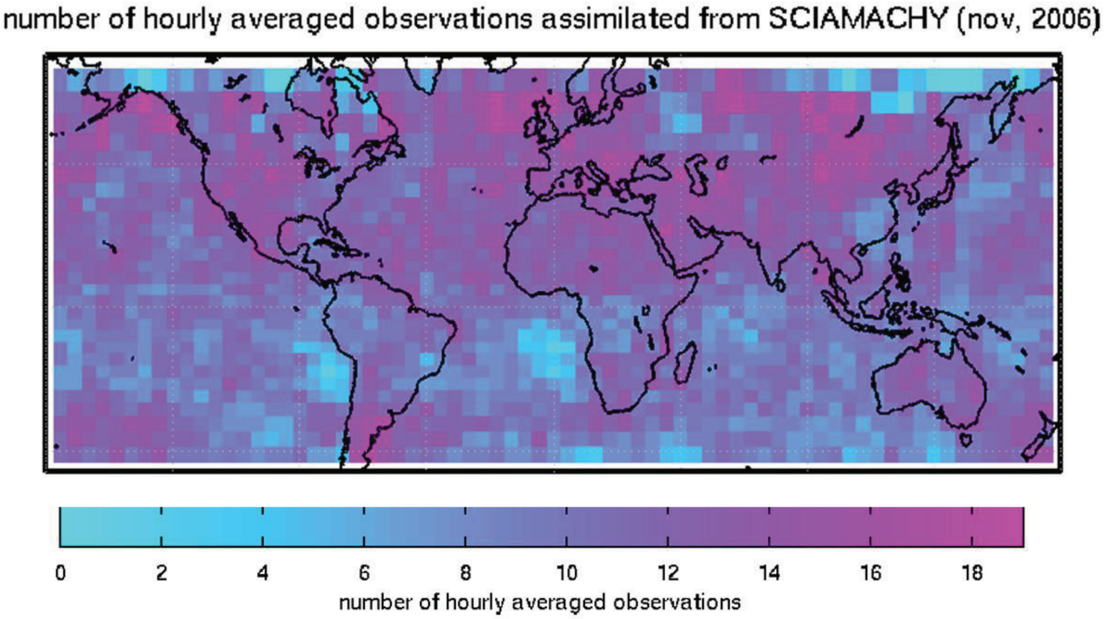

Figure 3.14: Number of observations assimilated into the inverse models. All co-located observations within the 4x5 resolution grid box occurring in the same hour were averaged. Observations with higher than 50% cloud coverage were eliminated.

The month-long 10am overpass was then repeated using the synthetic observations that had up to 30% random error added to them. However this time, observations that corresponded to the SCIAMACHY observations with cloud fractions above 50% were removed in both simulations. Figure 3.15 shows the results of these simulations as compared to the month long simulations where all observations were included.

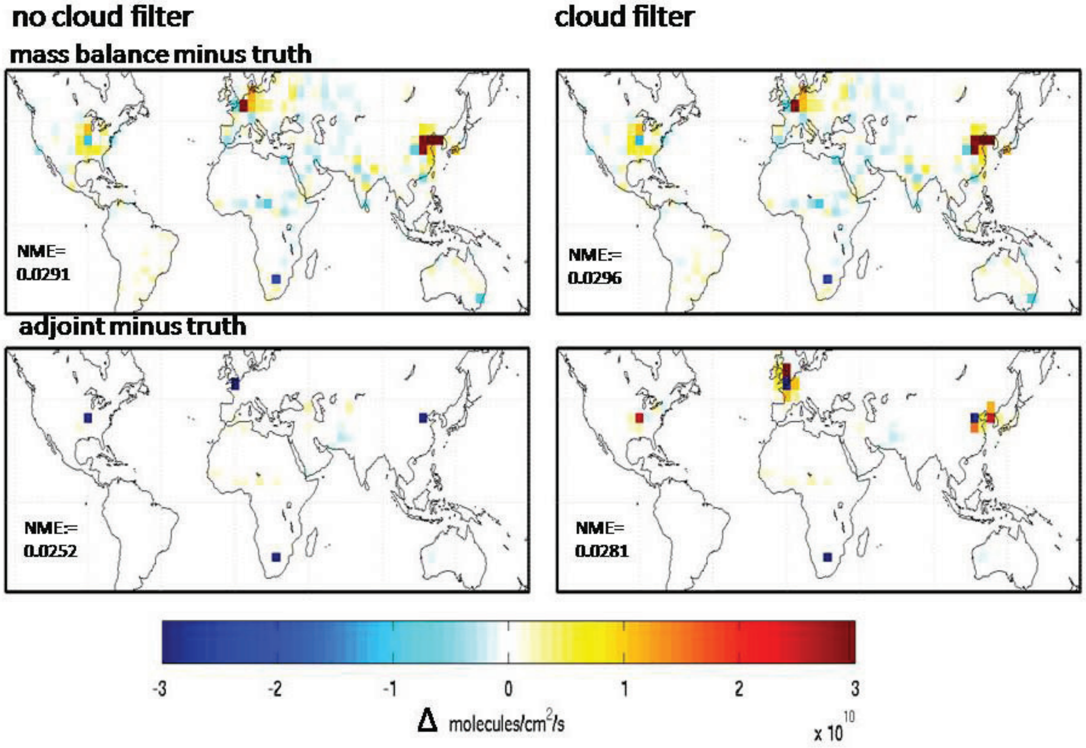

Figure 3.15: Absolute difference for *a posteriori* derived from mass balance inversions (top and adjoint inversions (bottom). "True" Emissions refer to GEOS-Chem simulations where surface NO_x in pixels over London, Beijing, Johannesburg, and the Ohio Valley have been doubled. A random error of 30% has been assigned to observations, which are sampled at 10 am local time every day in November, 2006. The left panels include all observations into the inversion and the right contains only those with less than a 50% cloud fraction.

The mass balance inversion is almost unaffected by the cloud filter. However, the cloud filter causes the adjoint inversion to be less effective at recovering emissions and resolving smearing.

3.2 Pseudo-Observations: EDGAR versus Regional Overwrites

It is unrealistic that true emissions and bottom up emissions would only differ at four points so another set of experiments was conducted. Observations at

10 am for everyday between November 15 and 21, 2006 were generated from a bottom-up inventory that included regional overwrites to the anthropogenic EDGAR emissions inventory. These overwrites were composed of the EPA/NEI99 for the US, EMEP for Europe, Streets *et. al* (2006) for southeast Asia, BRAVO for Mexico, and CAC for Canada. The observations were then inverted using a model that only had the global EDGAR inventory.

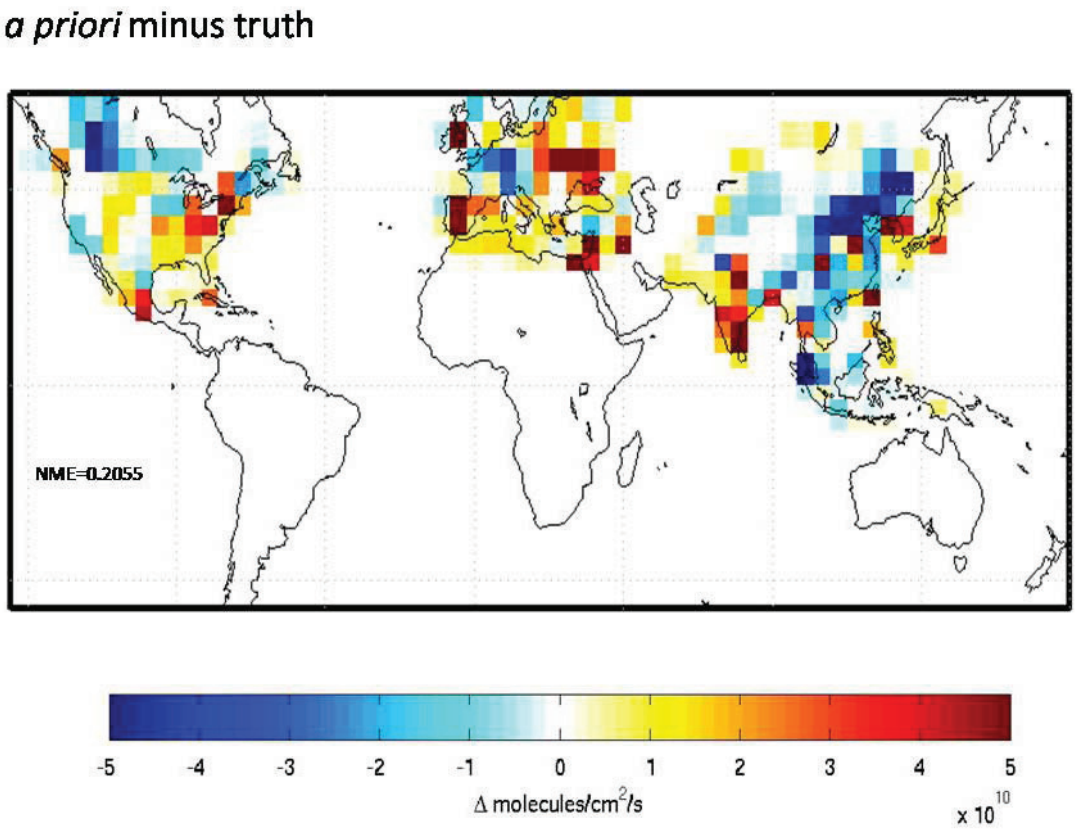

Figure 3.16: Absolute Difference between "true" emissions and a priori emissions. The a priori emissions use only the EDGAR inventory for anthropogenic NO_x emissions while the true emissions use regional overwrites to the EDGAR inventory. The time period is November 15-21, 2006.

Figure 3.16 shows the difference between the *a priori* bottom-up estimate of emissions and the true values along with the NME. The differences are primarily in the Northern Hemisphere. Figure 3.17 shows the results for both *a posteriori* estimates when observations are perfect and when observations have random noise added. When observations are perfect, the two methods have a very similar error. However, when random noise of up to 30% is used, the mass balance inversion recovers emissions better than the adjoint inversion. The mass balance method does not produce much error in the southern hemisphere, where true and perturbed emissions are the same. The adjoint method shows error in Africa, South America, and Australia. These areas are caused by noise in the observation, since there is no difference in emissions in these areas. The temporal averaging that occurs in the mass balance inversion could be better at cancelling the noise.

Both inversions agree in most regions, except over Europe and parts of Asia. The mass balance produces similar results as the *a priori*, showing higher and lower emissions (with respect to "true emissions") in the same areas. The adjoint inversion shows reverse signs in many of these areas.

The observations with up to 30% random noise were again assimilated using different time periods to test how the number of observations affects each method. Figure 3.18 shows the normalized mean error for each experiment. The number of observations has little effect on the mass balance inversions. The adjoint inversions generally do not recover the emissions as well as the mass balance inversion. The adjoint inversions do not improve in this case as number of observations increase. The introduction of noise seems to impair the adjoint method the most, which is indicated over Europe where areas that had higher emissions than the truth are now lower.

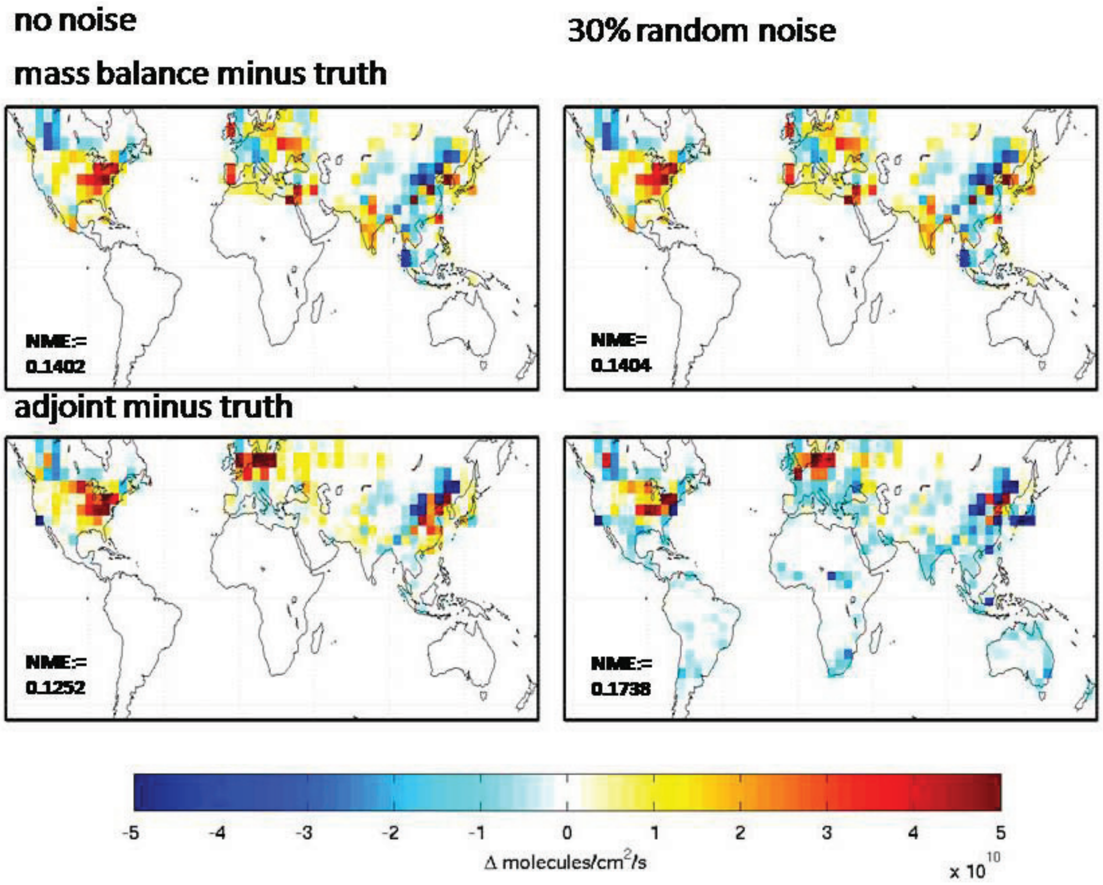

Figure 3.17: Absolute Difference between Mass Balance Approach and "truth" (left) and Absolute Difference between Adjoint Approach and "truth" (right) for perfect observations (top) and observation that 30% random noise (bottom) for Nov 15-21, 2006. The true emissions use regional overwrites to the EDGAR inventory, while the model only uses the EDGAR for anthropogenic emissions. Observations from 10am for each day were used.

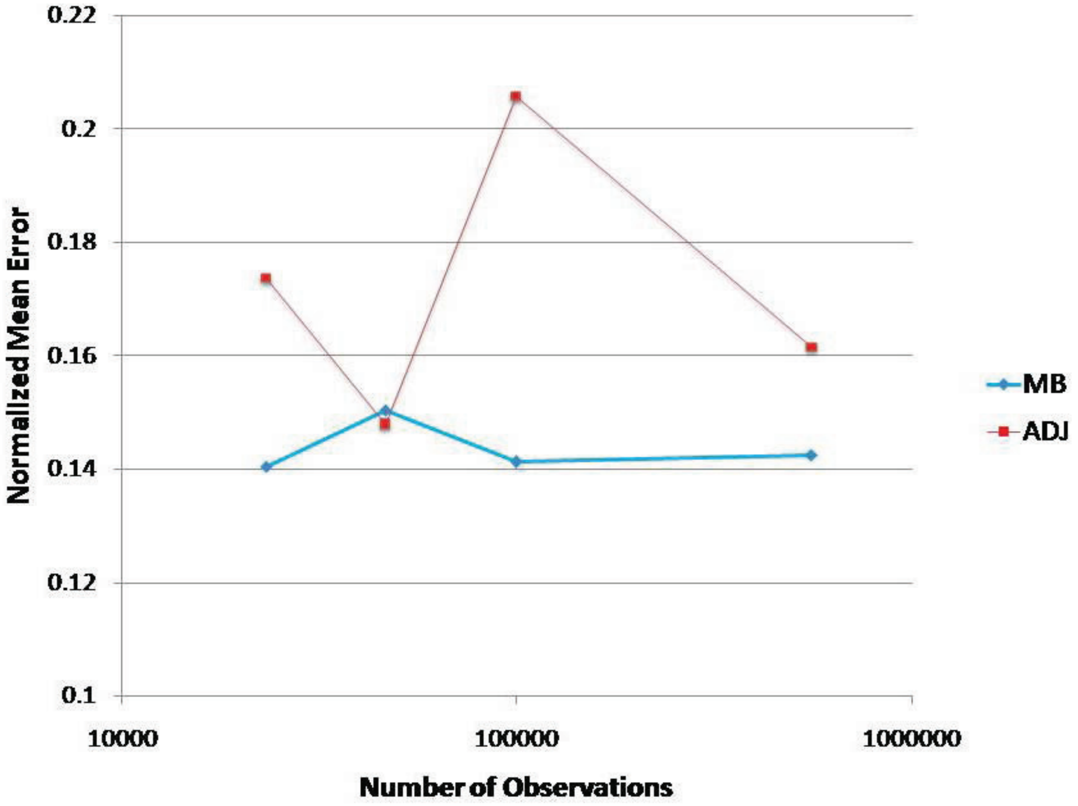

Figure 3.18: Normalized mean Error (NME) versus number of observations for November, 2006. Observations have up to 30% random noise added.

When observations were eliminated to represent missing observations due to cloud fraction, the mass balance had a slightly higher error. Figure 3.19 shows the results of the two methods- with and without the cloud filter. The mass balance inversion has a much lower error than the adjoint in both instances. The adjoint *a posteriori* emissions in both cases are better than the *a priori* emissions, which has an NME of 0.2264. The cloud filter improves the performance of the adjoint inversion in this case.

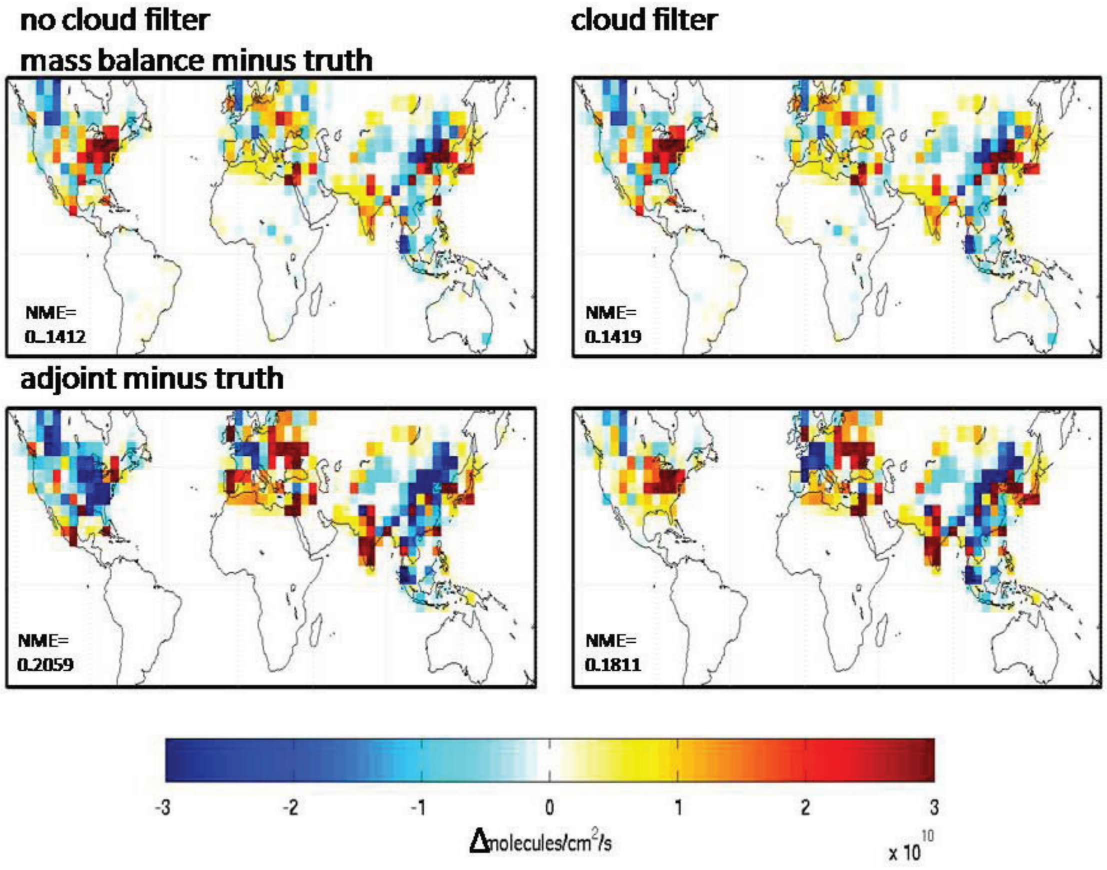

Figure 3.19: Absolute difference for *a posteriori* derived from mass balance inversions (top and adjoint inversions (bottom). The true emissions use regional overwrites to the EDGAR inventory, while the model only uses the EDGAR for anthropogenic emissions. A random error of up to 30% has been assigned to observations, which are sampled at 10 am local time every day in November, 2006. The left panels include all observations into the inversion and the right contains only those with less than a 50% cloud fraction.

3.3 Assimilating Satellite Observations

Observations from the SCIAMACHY satellite instrument for the year 2006 were used for further analysis. Observations from the SCIAMACHY instrument for July and November of 2006 were inverted using both methods. All observations with a cloud fraction lower than 50% for the entire month were used. The observations were re-gridded from SCIAMACHY resolution of 30 x 60km to 4°x5°. Figure 3.20 shows the results from July, 2006. The two figures on the left compare the modeled and observed columns.

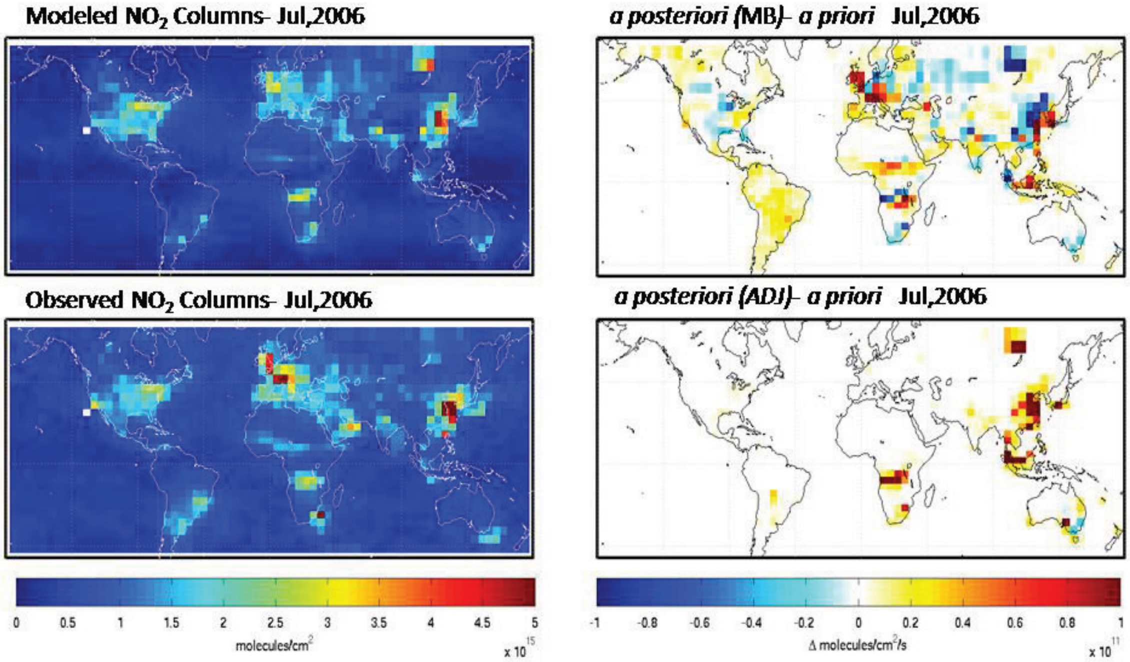

Figure 3.20: Results from Assimilating SCIAMACHY columns using both methods for July 2006. The first column shows the NO_2 columns and the second column shows the absolute difference between the *a posteriori emissions* and the *a priori.* The entire month of observations has been assimilated with an observational error of 30% and a perfect forward model. Observations with more than 50% cloud fraction have been removed.

In July, the observed and modeled NO_2 agree with each other, with some exceptions. In Europe there are some higher values observed than predicted in the model. This enhancement is captured in the mass balance inversion but not in the adjoint. Both inversions capture the enhanced NO_2 over Africa but the adjoint attributes it to two areas rather than several. The adjoint attributes the enhanced NO_2 in South America to increased emissions over 2 areas but the mass balance attributes the enhancement to emission increases over most of the continent. Over China, the mass balance shows an increase of emissions over some points and a decrease in others, while the adjoint only shows an increase.

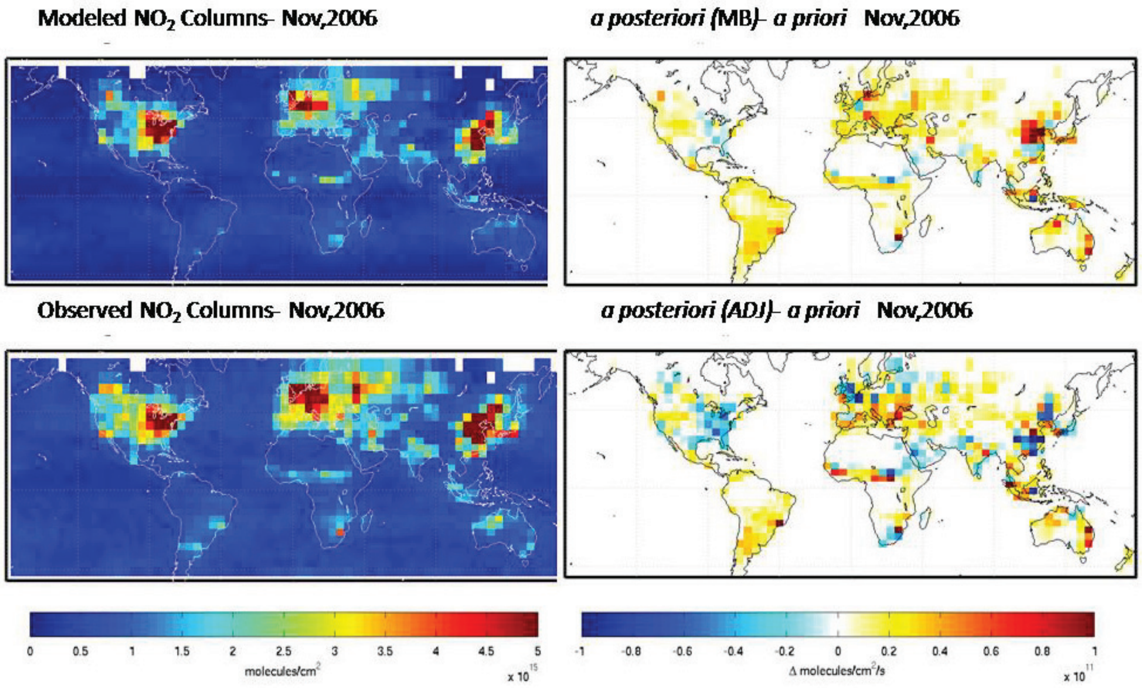

Figure 3.21:Results from Assimilating SCIAMACHY columns using both methods for November 2006. The first column shows the NO_2 columns and the second column shows s the absolute difference between the *a posteriori emissions* and the *a priori.* The entire month of observations has been assimilated with an observational error of 30% and a perfect forward model. Observations with more than 50% cloud fraction have been removed.

In November, it is expected that smearing will have a more significant role in the Northern hemisphere. The mass balance and adjoint inversions produce similar results. Over the Eastern United States, Western Europe, and China, the emissions from the adjoint inversion have slight differences than in the mass balance inversion. It was shown in the previous tests that smearing was better resolved by the adjoint inversion. Therefore this difference could indicate that smearing is taking place in the mass balance approach.

Figure 3.22 shows the *a posteriori* emissions derived from each approach for November and July. The correlation coefficient for the *a posteriori* inventories in November is 0.9529 and in July is 0.8253. There are some differences in the emissions derived from each approach. Overall though, these methods do appear to produce similar emissions estimates.

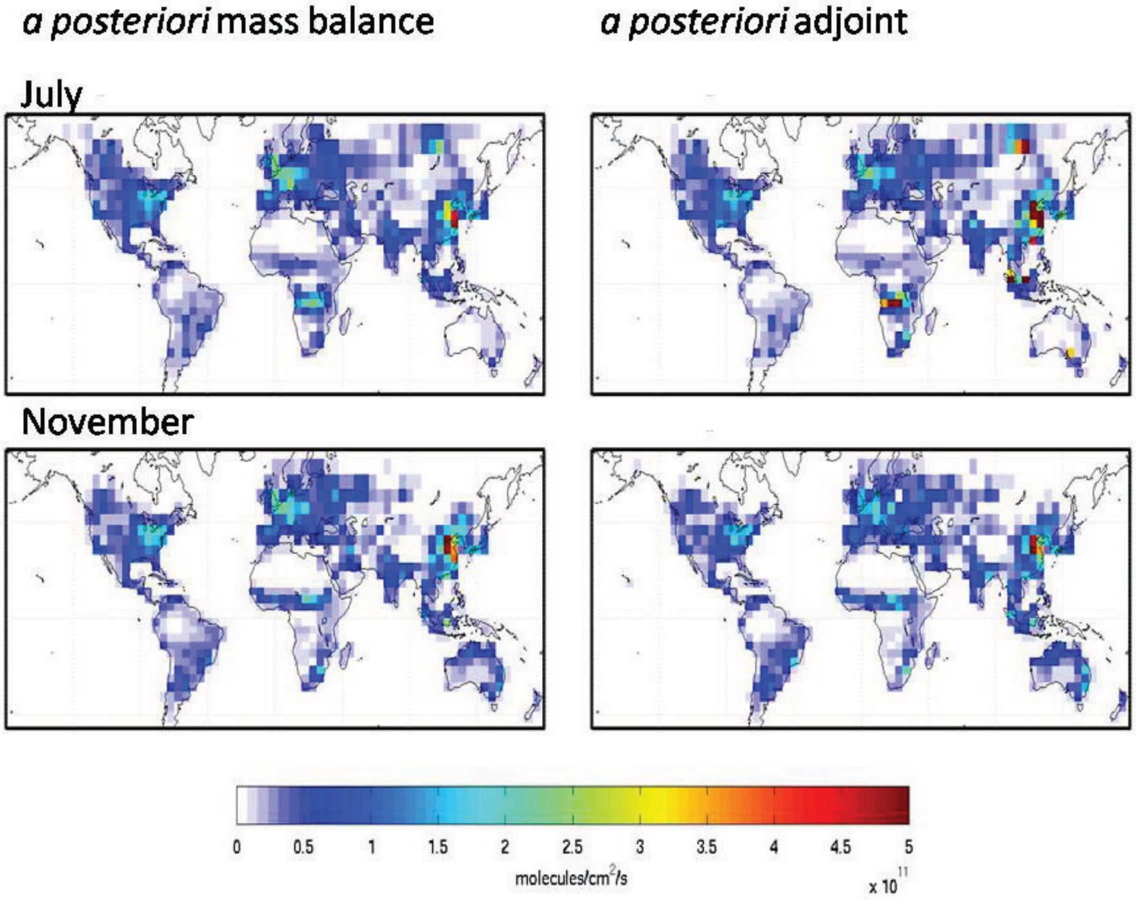

Figure 3.22: *A Posteriori* emissions derived from SCIAMACHY observations for November, 2006 and July, 2006. The left panels show the results derived from the mass balance approach while the right show those derived from the adjoint approach.

Chapter 4 Conclusions and Future Work

Two approaches have been used for inverting NO_2 observations to gain insight into NO_x emissions. The mass balance approach is based on the assumption of local photochemical steady-state for NO_2. The adjoint approach, an iterative approached based on Bayesian theory, optimizes emissions with the goal of minimizing the difference between modeled and observed columns. This study seeks to understand the differences between the two methods. Using both simulated and satellite-derived observations, inversions from both methods were explored.

An initial set of error–free synthetic observations was generated to test pixel smearing, or the influence of non-local NO_2 in the column due to transport from surrounding regions. The pseudo-observations differed from "true" observations at 4 points. The mass balance approach, even at a coarse 4x5 resolution, was shown to display smearing. The error increased during the winter by a factor of approximately 1.4, possibly due to smearing. The adjoint inversions were able to resolve the smearing better than the mass balance inversions, having errors that were an order of magnitude lower. The adjoint approach's performance improved when observations went from one hour of observations to one week of hourly observations, reducing the error by 2 orders of magnitude.

An iterative mass balance approach was tested to see if it could resolve smearing. Subsequent iterations pushed the *a posteriori* inventory closer to the top-down emissions estimate. This did not resolve the smearing.

Although the adjoint performed better than the mass balance in the previous tests, random noise affected this type of inversion. For the one-week simulations in November, the error in the adjoint inversion increased by from 0.017 to 0.13 when random noise of up to 30% was added to the observations. The normalized mean error in the mass balance inversion increased to a lesser extent from 0.019 to 0.051. The mass balance inversions had less noise, probably due to the averaging of observations over the time domain. Increasing the number of observations improved the adjoint's performance. Similar error increases occurred for simulations in July.

A second set of pseudo-observations were created. In this case emissions over most of North America were perturbed. When no noise was added to observations, the adjoint and mass balance performed similarly, differing in results over Europe and parts of Asia. In week-long simulations, when a random noise of up to 30% was added, the mass balance recovered the true emissions better, with an error of 0.14. The error in the adjoint inversion was 0.17.Neither approach was improved with more observations. Both approaches recovered emissions better than the *a priori*, which had an error of 0.21.

If the knowledge from these tests are applied to the inversions of SCIAMACHY NO_2 observations, the adjoint would perform better in areas where smearing is present and areas with low observational error. In July, smearing would be more present in the Southern Hemisphere and in November, in the Northern Hemisphere. SCIAMACHY satellite observations have an error of approximately 40% + 1.0 e15. However, if the number of observations assimilated is high, the error is reduced. Therefore, it is expected that the adjoint recovered the emissions better in areas where there were a large number observations and where smearing was a significant source of error. When inverting SCIAMACHY observations for July and November, both methods produced similar qualitative results.

At higher resolutions, higher smearing is expected in the mass balance approach. The adjoint would be useful in these conditions. However, as resolution increases, there are fewer hourly observations in each grid box. This could cause higher error in the observations, decreasing the effectiveness of the adjoint approach. Future work should explore the two methods at higher resolutions.

Overall, both methods were effective at improving the emissions inventory from the *a priori* model. The adjoint produced more accurate results in low noise situations and where smearing was present. The mass balance approach was 20-30 times faster, and seemed to handle noisy measurements better.

References

Bey, I., Jacob, D., Yantosca, R., Logan, J., Field, B., & Fiore, A. (2001). Global modeling of tropospheric chemistry with assimilated meteorology: Model description and evaluation. *Journal of Geophysical Research, 106*(D19), 23073.

Bogumil, K., Orphal, J., Homann, T., Voigt, S., Spietz, P., & Fleischmann, O. (2003). Measurements of molecular absorption spectra with the SCIAMACHY pre-flight model: Instrument characterization and reference data for atmospheric remote-sensing in the 230-2380 nm region. *Journal of Photochemistry and Photobiology.A, Chemistry, 157*(2-3), 167.

Bovensmann, , Burrows, , Frerick, , Chance, , Goede, , & Noel, . (1999). Global atmospheric monitoring with SCIAMACHY. *Physics and Chemistry of the Earth.Part C: Solar-Terrestrial and Planetary Science, 24*(5), 427.

Boylan, J. W., & Russell, A. G. (2006). PM and light extinction model performance metrics, goals, and criteria for three-dimensional air quality models. *Atmospheric Environment, 40*(26), 4946-4959. doi:10.1016/j.atmonsenv.2005.09.087

Burnett, R. T., Stieb, D., Brook, J. R., Cakmak, S., Dales, R., &Raizenne, M. (2004). Associations between short-term changes in nitrogen dioxide and mortality in canadian cities.*Archives of Environmental Health, 59*(5), 228.

Byrd, R. H., Lu, P. H., Nocedal, J., & Zhu, C. Y. (1995).A limited memory algorithm for bound constrained optimization. *SIAM Journal on Scientific Computing, 16*(5), 1190-1208. doi:10.1137/0916069

Chance, K. (1998).Analysis of BrO measurements from the global ozone monitoring experiment. *Geophysical Research Letters, 25*(17), 3335-3338. doi:10.1029/98GL52359

Daescu, D. N., Sandu, A., & Carmichael, G. R. (2003). Direct and adjoint sensitivity analysis of chemical kinetic systems with KPP: II - numerical validation and applications. *Atmospheric Environment, 37*(36), 5097-5114. doi:10.1016/j.atmosenv.2003.08.020

Damian, V., Sandu, A., Damian, M., Potra, F., & Carmichael, G. R. (2002).The kinetic preprocessor KPP - a software environment for solving chemical kinetics. *Computers & Chemical Engineering, 26*(11), 1567-1579. doi:10.1016/S0098-1354(02)00128-X

Evans, M. J., & Jacob, D. J. (2005). Impact of new laboratory studies of N(2)O(5) hydrolysis on global model budgets of tropospheric nitrogen oxides, ozone, and OH. *Geophysical Research Letters, 32*(9), L09813.doi:10.1029/2005GL022469

Forster, P., Freckleton, R., & Shine, K. (1997).On aspects of the concept of radiative forcing. *Climate Dynamics, 13*(7-8), 547.

Giering, R., & Kaminski, T. (1998). Recipes for adjoint code construction. *ACM Transactions on Mathematical Software, 24*(4), 437-474. doi:10.1145/293686.293695

Henze, D. K., Hakami, A., & Seinfeld, J. H. (2007). Development of the adjoint of GEOS-chem. *Atmospheric Chemistry and Physics, 7*(9)

Henze, D. K., Seinfeld, J. H., &Shindell, D. T. (2009). Inverse modeling and mapping US air quality influences of inorganic PM2.5 precursor emissions using the adjoint of GEOS-chem. *Atmospheric Chemistry and Physics, 9*(16)

Hudman, R. C., Jacob, D. J., Turquety, S., Leibensperger, E. M., Murray, L. T., Wu, S., et al. (2007). Surface and lightning sources of nitrogen oxides over the united states: Magnitudes, chemical evolution, and outflow. *Journal of Geophysical Research-Atmospheres, 112*(D12), D12S05.doi:10.1029/2006JD007912

Kuenen, J. J. P. (2006). Anthropogenic NO_xemission estimates for china based on satellite measurements and chemistry-transport modelling technical report: 2006. *Technical Report,*

Kurokawa, J., Yumimoto, K., Uno, I., &Ohara, T. (2009).Adjoint inverse modeling of NOx emissions over eastern china using satellite observations of NO2 vertical column densities. *Atmospheric Environment, 43*(11), 1878-1887. doi:10.1016/j.atmosenv.2008.12.030

Lamsal, L. N., Martin, R. V., van Donkelaar, A., Steinbacher, M., Celarier, E. A., Bucsela, E., . . . Pinto, J. P. (2008). Ground-level nitrogen dioxide concentrations inferred from the satellite-borne ozone monitoring instrument. *Journal of Geophysical Research-Atmospheres, 113*(D16), D16308.doi: 10.1029/2007JD009235

Lamsal, L. N., Martin, R. V., van Donkelaar, A., Celarier, E. A., Boersma, R. K., Dirksen, R., . . . Wang, Y. (2010). Indirect validation of tropospheric nitrogen dioxide retrieved from the OMI satellite instrument: Insight into the seasonal variation of nitrogen oxides at northern midlatitudes. *Journal of Geophysical Research, 115*doi: 10.1029/2009JD013351

Lin, J. -T. (2012).Satellite constraint for emissions of nitrogen oxides from anthropogenic, lightning and soil sources over east china on a high-resolution grid. *Atmospheric Chemistry and Physics, 12*(6), 2881-2898.doi:10.5194/acp-12-2881-2012

Martin, R., Chance, K., Jacob, D., Kurosu, T., Spurr, R., &Bucsela, E. (2002).An improved retrieval of tropospheric nitrogen dioxide from GOME. *Journal of Geophysical Research, 107*(d20), 4437.

Martin, R., Jacob, D., Chance, K., Kurosu, T., Palmer, P., & Evans, M. (2003).Global inventory of nitrogen oxide emissions constrained by space-based observations of NO2 columns. *Journal of Geophysical Research, 108*(d17), 4537.

Martin, R. V., Parrish, D. D., Ryerson, T. B., Nicks, D. K., Chance, K., Kurosu, T. P., et al. (2004). Evaluation of GOME satellite measurements of tropospheric NO2 and HCHO using regional data from aircraft campaigns in the southeastern United States. *Journal of Geophysical Research-Atmospheres, 109*(D24), D24307.doi:10.1029/2004JD004869

Martin, R. V., Sioris, C. E., Chance, K., Ryerson, T. B., Bertram, T. B., Wooldridge, T. H., et al. (2006). Evaluation of space-based constraints on global nitrogen oxide emissions with regional aircraft measurements over and downwind of eastern North America. *Journal of Geophysical Research, 111*(d15), D15308.

Mijling, B., & van der A, R. J. (2012).Using daily satellite observations to estimate emissions of short-lived air pollutants on a mesoscopic scale. *Journal of Geophysical Research-Atmospheres, 117*, D17302.doi:10.1029/2012JD017817

Napelenok, S. L., Pinder, R. W., Gilliland, A. B., & Martin, R. V. (2008). A method for evaluating spatially-resolved NO(x) emissions using kalman filter inversion, direct sensitivities, and space-based NO(2) observations. *Atmospheric Chemistry and Physics, 8*(18), 5603-5614.

Olivier, J. G. J. (2001). Applications of EDGAR.including a description of EDGAR 3.0: Reference database with trend data for 1970-1995. *RIVM Report no. 773301 001/NOP Report no. 410200 051,* Park, R. J., Jacob, D. J., Field, B. D., Yantosca, R. M., & Chin, M. (2004). Natural and transboundary pollution influences on sulfate-nitrate-ammonium aerosols in the United States: Implications for policy. *Journal of Geophysical Research-Atmospheres, 109*(D15), D15204.doi:10.1029/2003JD004473

Palmer, P. I., Jacob, D. J., Fiore, A. M., Martin, R. V., Chance, K., & Kurosu, T. P. (2003). Mapping isoprene emissions over north america using formaldehyde column observations from space, *Journal of Geophysical Research-Atmospheres,* doi: 10.1029/2002JD002153

Palmer, P., Jacob, D., Chance, K., Martin, R., Spurr, R., &Kurosu, T. (2001). Air mass factor formulation for spectroscopic measurements from satellites: Application to formaldehyde retrievals from the global ozone monitoring experiment. *Journal of Geophysical Research, 106*(D13), 14539.

Sandu, A., Daescu, D. N., & Carmichael, G. R. (2003). Direct and adjoint sensitivity analysis of chemical kinetic systems with KPP: Part I - theory and software tools. *Atmospheric Environment, 37*(36), 5083-5096. doi:10.1016/j.atmosenv.2003.08.019

Streets, , He, , Wang, , Richter, , Burrows, , & Zhang, . (2007). NOx emission trends for china, 1995-2004: The view from the ground and the view from space. *Journal of Geophysical Research, 112*(d22), D22306.

Streets, D. G., Zhang, Q., Wang, L., He, K., Hao, J., Wu, Y., et al. (2006).Revisiting china's CO emissions after the transport and chemical evolution over the pacific (TRACE-P) mission: Synthesis of inventories, atmospheric modeling, and observations.*Journal of Geophysical Research-Atmospheres, 111*(D14), D14306.doi:10.1029/2006JD007118

Turner, A. J., Henze, D. K., Martin, R. V., &Hakami, A. (2012). The spatial extent of source influences on modeled column concentrations of short-lived species. *Geophysical Research Letters, 39*, L12806.doi:10.1029/2012GL051832

Wild, O., Zhu, X., & Prather, M. J. (2000). Fast-j: Accurate simulation of in- and below-cloud photolysis in tropospheric chemical models. *Journal of Atmospheric Chemistry, 37*(3), 245-282. doi:10.1023/A:1006415919030

Yienger, J. J., & Levy, H. (1995).Empirical-model of global soil-biogenic NO_x emissions. *Journal of Geophysical Research-Atmospheres, 100*(D6), 11447-11464. doi:10.1029/95JD00370

Zhao, C., & Wang, Y. (2009). Assimilated inversion of NOx emissions over east asia using OMI NO2 column measurements. *Geophysical Research Letters, 36*, L06805.doi:10.1029/2008GL037123

Zhu, C., Byrd, R. H., Lu, P., &Nocedal, J. (1994).L-BFGS-B-fortran subroutines for large-scale bound constrained optimization. *technical report,nam-11,*